

Simulation and scaling analysis of periodic surfaces with small-scale roughness in turbulent Ekman flow

Jonathan Kostelecky^{1,2,†} and Cedrick Ansorge¹

¹Institut für Meteorologie, Freie Universität Berlin, Carl-Heinrich-Becker-Weg 6-10, 12165 Berlin, Germany

²Institut für Geophysik und Meteorologie, Universität zu Köln, Pohligstr. 3, 50969 Cologne, Germany

(Received 20 December 2023; revised 14 May 2024; accepted 30 May 2024)

Roughness of the surface underlying the atmospheric boundary layer causes departures of the near-surface scalar and momentum transport in comparison with aerodynamically smooth surfaces. Here, we investigate the effect of 56×56 homogeneously distributed roughness elements on bulk properties of a turbulent Ekman flow. Direct numerical simulation in combination with an immersed boundary method is performed for fully resolved, three-dimensional roughness elements. The packing density is approximately 10% and the roughness elements have a mean height in wall units of $10 \lesssim H^+ \lesssim 40$. According to their roughness Reynolds numbers, the cases are transitionally rough, although the roughest case is on the verge of being fully rough. We derive the friction of velocity and of the passive scalar through vertical integration of the respective balances. Thereby, we quantify the enhancement of turbulent activity with increasing roughness height and find a scaling for the friction Reynolds number that is verified up to $Re_\tau \approx 2700$. The higher level of turbulent activity results in a deeper logarithmic layer for the rough cases and an increase of the near-surface wind veer in spite of higher Re_τ . We estimate the von Kármán constant for the horizontal velocity $\kappa_m = 0.42$ (offset $A = 5.44$) and for the passive scalar $\kappa_h = 0.35$ (offset $\Delta = 4.2$). We find an accurate collapse of the data under the rough-wall scaling in the logarithmic layer, which also yields a scaling for the roughness parameters z -nought for momentum (z_{0m}) and the passive scalar (z_{0h}).

Key words: topographic effects, turbulent boundary layers, meteorology

† Email address for correspondence: j.kostelecky@posteo.de



1. Introduction

Roughness characterizes a plethora of turbulent flows at various scales – from the smallest scales encountered in geophysical flow (such as the roughness of individual surfaces, tree leaves, etc.) via the bulk roughness of real surfaces to the largest scales in the Earth system, where topographic undulations present a roughness for synoptic-scale systems. While under strong conditions on the surface properties, a flow can be considered hydraulically smooth (Pope 2000), atmospheric flows are virtually always rough due to the small-scale heterogeneity of the underlying Earth's surface in combination with the low viscosity of air. The atmospheric boundary layer (ABL) is the lowest part of the Earth's atmosphere with a thickness of 0.1 to 2 km (Garratt 1992) and a prototype rough ABL is the objective of this study.

Rotation of the Earth is a unique feature of the ABL; despite the small Rossby number, it causes significant departures in comparison with simpler canonical flows (e.g. closed channel or pipe flow). It is commonly considered by background rotation around the vertical axis – giving rise to Ekman flow (Ekman 1905). For a statistical two-point description of the flow, such rotation breaks the symmetry in the spanwise direction. Near the ground, surface friction comes into play and decelerates the flow, and the mean wind rotates in favour of the pressure gradient force, forming the Ekman spiral. Given the friction velocity u_τ and the Coriolis parameter f , the outer scale of the Ekman flow $\delta = u_\tau/f$, a scale for the boundary-layer thickness, forms as a consequence of shear growth and rotational suppression of the boundary layer; though unknown *a priori*, it is a constant for neutrally stratified flow and depends on the Reynolds number only – in stark contrast to spatially evolving boundary layers. Further, the turbulent boundary layer is complemented by an infinite reservoir of non-turbulent fluid aloft, which can be entrained into the boundary layer, causing departures of mean-flow statistics with respect to non-external canonical flows.

Direct numerical simulation (DNS) of Ekman flow is a viable model for ABL turbulence. Following the seminal work of Coleman, Ferziger & Spalart (1990), it was studied for hydraulically smooth configurations (Coleman 1999; Shingai & Kawamura 2004; Miyashita, Iwamoto & Kawamura 2006; Spalart, Coleman & Johnstone 2008, 2009; Ansorge & Mellado 2014, 2016; Deusebio *et al.* 2014; Shah & Bou-Zeid 2014; Ansorge 2019). Considerations over non-smooth surfaces are scarce: to the authors' knowledge, Lee, Gohari & Sarkar (2020), who conduct DNS of the Ekman flow for sinusoidal surface topography under neutral and stable density stratification, is the only example. They investigate two-dimensional periodic bumps with $H^+ = 15$ at $Re_\tau = 700$, where H^+ is the height of the bumps in viscous units and Re_τ the friction Reynolds number, i.e. in the transitionally rough regime and find increased turbulent kinetic energy (TKE) production with an increasing slope of the bumps – counteracting buoyancy-induced suppression of turbulence. Limitations of the study are the absence of sharp edges, thus limiting flow instability and flow turbulence enhancement, the two-dimensional shape of their roughness elements and limited scale separation (Re_τ). Here, we complement this approach by (i) adding square surface elements to represent the small-scale roughness over homogeneous surfaces encountered frequently underneath the ABL and (ii) by an increased scale separation.

The effect of a rough boundary in turbulent flow is reviewed by Raupach, Antonia & Rajagopalan (1991), Finnigan (2000), Jiménez (2004), Kadivar, Tormey & McGranaghan (2021) and Chung *et al.* (2021). Homogeneously rough flow, i.e. flow with a statistically homogeneous description of the roughness elements, is governed by two dimensionless

parameters: (i) a roughness Reynolds number

$$H^+ = \frac{H}{\delta_v}, \tag{1.1}$$

where H is the height of roughness, $\delta_v = \nu/u_\tau$ the viscous length scale with u_τ the friction velocity and ν the kinematic viscosity, and (ii) the blocking ratio H/δ , where δ is the boundary-layer thickness. Different roughness regimes are encountered for increasing H^+ , ranging from hydraulically smooth – where no roughness effects are found in the flow statistics above the viscous layer – via transitionally rough to fully rough – where pressure drag outweighs the skin frictional drag and the buffer layer is replaced by a roughness sublayer. Values for the regime transitions are reported based on experiments (cf. table 2 in Kadivar *et al.* 2021). These are based on the pioneering work of Nikuradse (1933), who studied pipe flow with uniform sand-grain roughness and on the later work by Schlichting (1936), who introduced the equivalent sand-grain roughness with the aim of transferring Nikuradse’s theory to other roughness geometries. In essence, the latter work suggests there exists an approximate scale z_{0m} representing roughness effects also for less ideal configurations. This equivalent parameter, the aerodynamic roughness length for momentum z_{0m} , defines an empirical roughness Reynolds number z_{0m}^+ which is commonly used in studies of rough configurations. The ABL flow is considered hydraulically smooth flow for $z_{0m}^+ \lesssim 0.135$ and fully rough for $z_{0m}^+ \gtrsim 2 - 2.5$ with the transitionally rough regime in between (Brutsaert 1982; Andreas 1987). The zero-plane displacement height d reflects a virtual shift of the effective underlying surface for high packing densities when fitting the logarithmic law. In the essence of classical scaling theory, the logarithmic law of the wall for the mean velocity $\bar{u}(z)$ under neutral conditions is

$$\bar{u}(z) = \frac{u_\tau}{\kappa} \ln \left(\frac{z}{z_0} \right), \tag{1.2}$$

following the notation of Monin (1970) (cf. their equation 9a), with the von Kármán constant κ . For flow over rough surfaces, z is substituted by $z - d$ (in 1.2), for consideration of the zero-plane displacement height d . This form of the logarithmic law – with the roughness parameter z_0 – forms the cornerstone of the Monin–Obukhov similarity theory (MOST, cf. Monin 1970; Foken 2006).

The second parameter of the roughness, the blocking ratio H/δ , can be used to describe the influence of roughness on the logarithmic layer and wall similarity (based on Townsend 1961, 1976, and elaborated by Raupach *et al.* 1991). Jiménez (2004) found that wall similarity holds if $\delta/H > \delta_{crit}/H$ for $\delta_{crit}/H \approx 40-80$. Notably, for the friction Reynolds number $Re_\tau = \delta^+$, it is

$$Re_\tau = \frac{\delta}{H} H^+ = \delta^+. \tag{1.3}$$

However, this suggests that the total turbulent scale separation measured in terms of Re_τ is to be considered as geometrically composed of, first, a separation between large eddies and the roughness scale and, second, a separation between the roughness scale and viscosity. The scale separation between the inner viscous scale δ_{inner} and the outer scale δ_{outer} of the problem in a general formulation is given as

$$Re_{gen} = \frac{\delta_{outer}}{\delta_{inner}} = \frac{\delta}{F(\delta_v, H)}, \tag{1.4}$$

in the form of the general-Reynolds number Re_{gen} . In the smooth limit, it is $\delta_{inner} \sim \delta_v$, Re_{gen} is the friction Reynolds number Re_τ . However, in the fully rough limit $\delta_{inner} \sim H$

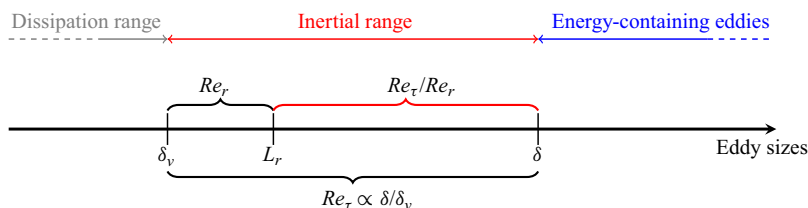


Figure 1. Schematic of the scale separation in a turbulent flow as a function of the eddy sizes, with roughness acting at a range of scale $O(L_r)$. The energy-containing eddies are $O(\delta)$ for a turbulent Ekman layer and the onset of the dissipation range is located at $O(\delta_v)$, with the viscous scale $\delta_v = \nu/u_\tau$. The Reynolds numbers Re_τ and Re_r in this schematic give rise to a reduced Reynolds number $Re_\tau \propto Re_\tau/Re_r$, capturing the scale separation available for large-scale eddies until they hit the effects of bulk roughness.

and Re_{gen} is the blockage ratio δ/H . An overlap and logarithmic layer is only present if the scale separation in terms of Re_{gen} is sufficiently large.

When interpreting turbulent Ekman flow as an idealized representation of the ABL, a DNS approach inevitably resorts to the concept of Reynolds-number similarity: the scale separation necessary for a direct representation of geophysical problems at scale is out of reach, even using the most modern computational approaches. The common representation of a prototype turbulent flow shows a cascade of motions from large-scale energy-containing eddies to the dissipation range (figure 1). If there is sufficient scale separation in between the two, the inertial range develops a self-similar scaling. In this regime of fully developed turbulence, i.e. when a sufficiently large inertial range exists (Dimotakis 2005), the spectral properties are well described by the seminal theory put forward by Kolmogorov (1941) and Obukhov (1941). Further, some statistics of the flow – in particular low-order statistics, such as dissipation (Dimotakis 2005) and mean velocity profiles (Barenblatt 1993) – will cease to depend on the separation of scales, viz. Reynolds number. While these scales, and thus also Re_τ , exist and bear a physical meaning in the rough configuration, the roughness parameter L_r (characteristic roughness length scale) defines a new length scale. For all problems of relevance, it is $L \gg L_r$, with L the scale of the largest eddies and in our specific problem we identify $L \sim O(\delta)$ with the boundary-layer thickness, and $L_r \gtrsim O(\delta_v)$ (if $L_r \ll \delta_v$, the surface must be aerodynamically smooth; and if L_r reaches $O(\delta)$, an obstacle is no longer considered a roughness element). In analogy to the decomposition of the Reynolds number Re_τ proposed above (1.3), this gives rise to a roughness Reynolds number $Re_r \propto L_r/\delta_v$ which can be interpreted as a range of eddy sizes locally ‘occupied’ by roughness. This range is not available for an undisturbed continuation of the inertial range as roughness alters the scales of turbulent production, as measured by u_τ , and local dissipation of turbulence kinetic energy (Davidson & Krogstad 2014). From the perspective of large-scale motions, this limitation is similar to reducing the Reynolds number by $O(Re_r^{-1})$. In our study we will hence resort to cases with $Re_r = O(1)$ such that the turbulence instability of the large-scale eddies is retained despite the intermediate Reynolds number achieved in our DNS. While this limits us to relatively small roughness elements, we retain a proper turbulent interaction between the inner and outer scales as is observed in the real-world ABL.

The investigation of roughness gives rise to a huge parameter space, as the geometry, distribution and arrangement of roughness elements impact on the turbulent flow (Kadivar *et al.* 2021). Cubical roughness elements are one preferred set-up for studying the effect of three-dimensional roughness on wall-bounded turbulent flow in vegetation and urban canopies, and we choose them also here as the building blocks of the rough surface.

There are several numerical studies with staggered or aligned arrays, varying the roughness density and the size of roughness elements. The problem is investigated through DNS for channel flow (Coceal *et al.* 2006; Leonardi & Castro 2010), and for a turbulent boundary layer (Lee, Sung & Krogstad 2011*b*). It was also assessed by large-eddy simulation (LES) (Stoesser *et al.* 2003; Kanda, Moriwaki & Kasamatsu 2004; Cheng & Porté-Agel 2015) and through wind tunnel measurements (Castro 2007; Cheng *et al.* 2007; Perret *et al.* 2019). Coceal *et al.* (2006) emphasize the difference between two- and three-dimensional roughness: mixing and transport are different for a two-dimensional setting. For flow orthogonal to the elements, there are unrealistically large sheltering effects; for flow parallel to elements, secondary motions become unrealistically large. Furthermore, their findings imply that a variable height of the roughness elements is needed to capture real-world conditions. Indeed, LES studies of Xie, Coceal & Castro (2008) and Yang *et al.* (2016), investigated flows over blocks with a Gaussian height distribution. In this study, we chose blocks with a uniform height and width distribution to represent the randomness of individual roughness elements. Individual roughness elements are randomly offset from an equidistant, regular grid to also break symmetry due their positioning. The height of roughness elements can be considered with respect to the outer scale δ (giving rise to the blocking ratio) and the inner scale ν/u_τ (yielding the roughness Reynolds number H^+ ; cf. (1.3)). The present work is limited to rectangular roughness blocks with a small blocking ratio ($H/\delta \lesssim 1.5\%$) such that sufficient scale separation exists for a logarithmic layer to form.

The packing density of roughness elements – and hence the mutual sheltering– gives rise to three different flow regimes: isolated roughness, wake interference and skimming flow (Hussain & Lee 1980; Grimmond & Oke 1999). In the skimming regime, the packing density is sufficiently high such that the flow ‘slides’ over the roughness crests. In the other extreme case, the isolated roughness, the flow interaction between roughness elements is negligible and roughness elements can be considered as individual bluff bodies. Leonardi & Castro (2010) found the drag maximum for a packing density of 15%, which is in agreement with Kanda *et al.* (2013), whereas Ahn, Lee & Sung (2013) measured a value of 11.1% to 12.5% and Cheng & Porté-Agel (2015) a value of 10%. In the present study, we use a packing density of approximately 10%, which falls in between isolated and wake interference roughness according to Grimmond & Oke (1999) (cf. their figure 1).

In the current work, we aim to answer the following research questions regarding the quantitative effects of surface roughness on a prototype ABL: (i) What is the impact of a controlled and fully resolved surface roughness on bulk parameters and mean flow properties in the inner and outer layer? (ii) Do the rough-wall scaling and log-layer scaling follow the expected and widely used approaches in MOST for neutral conditions? (iii) Can we arrive at meaningful estimates for the zero-plane displacement and roughness length for momentum and scalar? (iv) How different is the enhanced mixing of the momentum and of the scalar in the presence of surface roughness? To do so, we extend a well-established modelling set-up for turbulent Ekman flow by an immersed boundary method (IBM) and deploy the problem on the supercomputing system Hawk at Höchstleistungsrechenzentrum Stuttgart (HLRS, Germany) to reach scale separation of up to $Re_\tau \approx 2700$.

2. Methodology

We consider Ekman flow of an incompressible fluid over a horizontal plate on the f -plane, that is, the Coriolis force only affects the horizontal velocity components and is constant. Far away from the wall, shear effects vanish and the flow is in geostrophic equilibrium, i.e. the pressure gradient is balanced by the Coriolis force.

2.1. *Governing equations and parameters*

The three-dimensional Navier–Stokes equations are numerically solved for an incompressible, Newtonian fluid with constant fluid properties (density ρ , viscosity ν) subject to steady system rotation about the vertical axis. The problem is discretized on the Cartesian coordinate system $X_i = (X, Y, Z)^T$, where X, Y is the streamwise, spanwise and Z the wall-normal coordinate, and we solve it on a cubic domain of size $[0, 0, 0] \leq [X, Y, Z] \leq [L_x, L_y, L_z]$. The streamwise direction is defined with respect to the smooth-wall flow; the flow direction deviates with increasing height and surface roughness. The dynamical system is governed by the following parameters: (i) the geostrophic wind vector $\mathbf{G} = (G_1, G_2, 0)^T$ and force $G = \sqrt{G_1^2 + G_2^2}$, and (ii) the Coriolis parameter f . Both scales yield the Rossby radius $\Lambda_{Ro} = G/f$ as a length scale. Thus, the governing flow equations are non-dimensionalized with the characteristic scales G, f, Λ_{Ro} and read

$$\frac{\partial u_i}{\partial x_i} = 0, \quad \frac{\partial u_i}{\partial t} + u_j \frac{\partial u_i}{\partial x_j} = -\frac{\partial \pi}{\partial x_i} + \frac{1}{Re_\Lambda} \frac{\partial^2 u_i}{\partial x_j^2} + f \epsilon_{ijk}(u_k - g_k). \tag{2.1a,b}$$

Here, t is the non-dimensional time, $\mathbf{u} = (u, v, w)^T = (u_1, u_2, u_3)^T$ is the non-dimensional velocity vector, $x_i = (x, y, z)^T$ the non-dimensional coordinates and $\partial \pi / \partial x_i$ the non-dimensional, non-hydrostatic, ageostrophic pressure gradient. Further, $\mathbf{g} = (g_1, g_2, 0)^T$ with $g_j = G_j/G$ is the normalized geostrophic wind (by construction $g = \|\mathbf{g}\| = 1$) and ϵ_{ijk} is the alternating unit tensor. The boundary conditions for the velocities are no slip at the bottom and free slip at the top boundary; periodic boundary conditions are applied in the horizontal directions. Equations (2.1b) solely depend on the Reynolds number $Re_\Lambda = \Lambda_{Ro}G/\nu$. For comparison with other studies, we refer to the Reynolds number

$$Re_D = \frac{GD}{\nu} = \sqrt{2Re_\Lambda}, \tag{2.2}$$

with $D = \sqrt{2\nu f^{-1}}$ the laminar Ekman layer thickness. Both Rossby and Ekman scalings lose their relevance once the system is in a fully turbulent state. Then, the system is scaled by the friction velocity u_τ (non-dimensionalized form $u_\star = u_\tau/G$), the turbulent boundary-layer thickness $\delta = u_\tau/f$ (non-dimensionalized form $\delta_\star = \delta/\Lambda_{Ro} = u_\star$) and the eddy-turnover scale f^{-1} . These turbulent scales result in the friction Reynolds number $Re_\tau = u_\tau \delta / \nu$ with

$$u_\star^2 = \frac{1}{Re_\Lambda} \sqrt{\left(\left.\frac{\partial \langle u \rangle}{\partial z}\right|_{z=0}\right)^2 + \left(\left.\frac{\partial \langle v \rangle}{\partial z}\right|_{z=0}\right)^2}, \tag{2.3}$$

such that Re_τ equals the non-dimensional wind-speed gradient at the surface. The definition (2.3) of u_\star is valid for a smooth wall located at $z = 0$. Over a non-flat surface, it is $u_\star^2 = \|\boldsymbol{\tau}_w\|/(\rho G^2) = \|\boldsymbol{\tau}_\star\|$, where $\boldsymbol{\tau}_w$ is the total surface shear stress (non-dimensional form $\boldsymbol{\tau}_\star$) and ρ the constant fluid density. As a consequence of rotation, the surface shear stress is not aligned with the geostrophic wind vector and the wind veers towards the surface as

$$\alpha(z) \triangleleft (\overline{\mathbf{u}}(z), \mathbf{g}) \quad \text{and} \quad \alpha_\star \triangleleft (-\boldsymbol{\tau}_\star, \mathbf{g}). \tag{2.4a,b}$$

The values u_\star, α_\star and δ_\star are unknown *a priori* but can be approximated as functions of Re_D (Spalart 1989). In external flow, there is a duality of scales, where the inner layer scales in inner units and the corresponding normalized quantities are denoted by $(\cdot)^+$, while the

outer layer scales in outer units, denoted by $(\cdot)^-$. The non-dimensional length and velocity scales are defined as

$$x_i^+ = x_i u_\star Re_\Lambda = \frac{X_i}{\delta_v}, \quad u_i^+ = \frac{u_i}{u_\star}, \quad x_i^- = \frac{x_i}{u_\star} = \frac{X_i}{\delta}, \quad u_i^- = u_i. \quad (2.5a-d)$$

The scalings are mapped by $x_i^+ = Re_\tau x_i^-$ and $u_i^- = u_\star u_i^+$. Spatial averaging of flow variables in the horizontal is denoted by $\langle (\cdot) \rangle$ and temporal averaging by $\overline{(\cdot)}$.

Along with the conservation equation of momentum, we solve the transport equation of a passive scalar s . Boundary conditions for the passive scalar are of Dirichlet type, with a constant difference between the lower and upper walls $\Delta s = s|_{z=L_z} - s|_{z=w}$, with $s|_{z=L_z} = 1$ and $s|_{z=w} = 0$. The conservation equation of the scalar is non-dimensionalized with the additional characteristic scale Δs , and it reads as

$$\frac{\partial s}{\partial t} + u_j \frac{\partial s}{\partial x_j} = \frac{1}{Re_\Lambda Sc} \frac{\partial^2 s}{\partial x_j^2}, \quad (2.6a)$$

with

$$Sc = \frac{\nu}{\kappa_d}, \quad (2.6b)$$

where Sc is the Schmidt number and κ_d the constant molecular diffusivity for the scalar. Analogously to the friction velocity we define a non-dimensional reference friction value for the scalar with

$$s_\star = \frac{q_\star}{u_\star} \quad \text{and} \quad q_\star = \frac{1}{Re_\Lambda Sc} \left. \frac{\partial s}{\partial z} \right|_{z=0}, \quad (2.7a,b)$$

where q_\star is the surface flux of the scalar for a smooth surface at $z = 0$. The scalar in inner units is given by $s^+ = s/s_\star$ and in outer units by $s^- = s$, since s is scaled by Δs .

Following Ansgore (2017), a Rayleigh-damping layer is introduced on the uppermost 20 grid points to suppress spurious boundary effects, that may occur as a consequence of a finite domain height.

2.2. Intrinsic averaging

Intrinsic averaging implies that only values inside the fluid domain are considered for averaging, in contrast to extrinsic averaging, where all values in the whole domain are taken into account. Since there is a mismatch between the volume share covered by roughness elements (figure 2a, red and blue shaded area) and the corresponding share of grid points, a volume approach (figure 2b) yielding a fluid fraction for the volume in the box around each grid point is used and described in detail in Appendix A. In this study, we apply intrinsic averaging to all mean vertical profiles and global flow parameters, within the roughness layer $z \leq H_{max}$, where H_{max} is the height of the largest roughness element.

2.3. Numerical approach of the DNS code

Simulations in this study use the open source DNS code `tlab` (<https://github.com/turbulencia/tlab>). The governing equations are advanced in time with a fourth-order five-stage low-storage Runge–Kutta scheme (Williamson 1980). Spatial derivatives are computed with finite differences of sixth-order accuracy (Lele 1992). Biased compact schemes of reduced order are used at the vertical (non-periodic) boundaries. The applied discretization results in an overall fourth-order accuracy of the code. Incompressibility

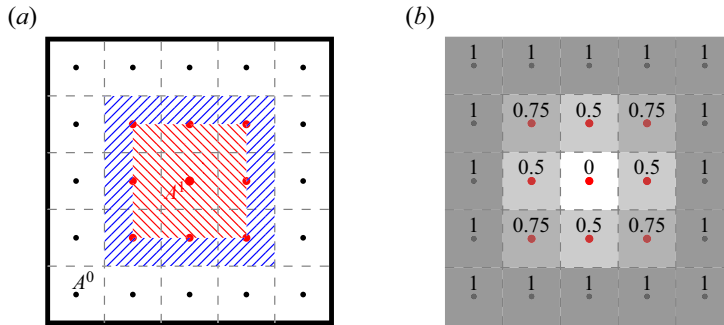


Figure 2. (a) Two-dimensional schematic of a solid object (red points) covering the area A^1 immersed in a fluid domain (black points) covering the area A^0 . The blue-shaded area belongs to the fluid, but field values in the area would be represented by the value on the solid surface. (b) Corresponding indicator field with volume fractions of the fluid $\epsilon^F(x_i) = [1 - \epsilon^S(x_i)]$.

is enforced with the fractional step method (Chorin 1968; Témam 1969) to ensure divergence-free velocity fields up to machine accuracy. The Poisson solver uses a Fourier-spectral approach in the periodic horizontal directions, and an inverse-compact approach along the vertical (Mellado & Ansoerge 2012). Originally, pressure and velocities are computed on the same grid in `tlab`. This collocated arrangement is well known to cause spurious pressure oscillations (Laiyet & Lamballais 2009) in combination with an IBM. Hence, the existing code was extended by a partially staggered pressure grid in the horizontal and a compact filter (Lele 1992) for the pressure in the vertical to circumvent the deterioration of the data by numerical artefacts in the pressure.

2.4. Immersed boundary method

The representation of flow obstacles with vertical walls and rigid boundaries challenges DNS codes of high-order accuracy and may cause numerical artefacts, referred to as spurious force oscillations (SFOs). With the aim of using Cartesian grids, an IBM is implemented in `tlab` and tested against reference data to ensure sufficient resolution and absence of SFOs that deteriorate the flow statistics.

The Gibbs phenomenon and SFOs are known artefacts to occur in moving-body problems (Lee *et al.* 2011a), but also for non-moving bodies represented through an IBM (Li, Bou-Zeid & Anderson 2016). The SFOs appear as high-frequency oscillations near a solid boundary (Fornberg 1996, p. 11). They can severely deteriorate the numerical solution. Not only may this impact instantaneous realizations of the flow, but also the long-time averages of flow quantities. In our case of rigid bodies represented by an IBM, SFOs are caused by a stepwise signal of the IBM forcing at the solid boundary in combination with a spectral-like compact differencing scheme. The oscillations may contaminate the flow field due to the non-local character of these schemes. Filtering and smoothing procedures in physical and frequency space can be used to reduce or control SFOs (Goldstein, Handler & Sirovich 1993; Kim, Kim & Choi 2001; Lamballais & Silvestrini 2002; Tseng, Meneveau & Parlange 2006; Fang *et al.* 2011).

The direct forcing IBM approach was introduced by Mohd-Yusof (1997) and Fadlun *et al.* (2000). It tries to avoid SFOs through an artificial flow in the solid regions that reduces discontinuities at the interface while fulfilling the boundary conditions. This leaves the external flow unaffected by the artificial flow (Fadlun *et al.* 2000). While the method was extended towards higher-order derivative schemes (Parnaudeau *et al.* 2004, 2008),

it remains limited to simple geometries like cylinders, and is problematic for objects with sharp edges (Giannenas & Laizet 2021, figure 2 on p. 610).

The alternating direction reconstruction (ADR) IBM, proposed by Gautier, Laizet & Lamballais (2014), allows simulations with more complex geometries while preserving the homogeneity of spatial operators. The flow is artificially expanded into solid regions to ensure the smoothness of fields across the interface, while the boundary conditions $u_i|_{interface} = 0$ are met. Gautier *et al.* (2014) used one-dimensional Lagrangian polynomials for interpolation, which are evaluated in the respective direction before a spatial derivative of the governing equations is evaluated in this direction. This procedure is repeated anew for each derivative and the values within the solid regions are not considered for subsequent calculations.

Lagrangian polynomials suffer from Runge’s phenomenon (Runge 1901), where large amplitudes occur at the boundaries for equidistant grids. As objects get wider, numerical instabilities can occur due to unphysically large derivatives at the interface and corresponding large pressure signals inside the solid. Giannenas & Laizet (2021) use cubic splines, avoiding the Runge phenomenon at boundary nodes, which results in reduced amplitudes of the auxiliary field within the solid. They demonstrate that the ADR IBM with cubic splines is well suited for sixth-order compact schemes and does not degrade the overall convergence order of the DNS code. Further, no additional stability constraints emerge and the computational overhead is marginal. Finally, the ADR IBM is highly scalable on high-performance computing systems, as the communication overhead of the parallel algorithm does not increase.

The ADR IBM is well tested for flow around a cylinder against both experimental and simulation data (Parnaudeau *et al.* 2008; Gautier, Biau & Lamballais 2013; Gautier *et al.* 2014; Giannenas & Laizet 2021) and across different DNS codes (Schäfer *et al.* 2020; Theobald *et al.* 2021). More recently, the ADR IBM was also applied for moving objects (Giannenas & Laizet 2021), to wavy channel turbulence (Khan & Jayaraman 2019; Jayaraman & Khan 2020), jet control with microjets (Gautier *et al.* 2014), LES of a circular cylinder wake flow (Resseguier *et al.* 2017; Chandramouli *et al.* 2018), flow over periodic hill (Xiao *et al.* 2020) and to channel flow over streamwise-aligned ridges (Schäfer *et al.* 2019) and with free convection (Schäfer *et al.* 2022b).

The implementation of the ADR IBM based on cubic splines in `tlab` enables DNS of Ekman flow with fully resolved roughness. An indicator field $\epsilon(x_i)$ is used to fully describe the spatial properties of the immersed roughness geometry in the computational domain Ω , which is decomposed into the solid and interface $\Omega_{\mathbb{S}}$ and fluid $\Omega_{\mathbb{F}}$ regions (figure 2), given by

$$\epsilon(x_i) = \begin{cases} 1, & \text{if } x_i \in \Omega_{\mathbb{S}}, \\ 0, & \text{if } x_i \in \Omega_{\mathbb{F}}. \end{cases} \quad (2.8)$$

Objects are bound to the location of the grid node positions, where the outer grid nodes labelled as solid represent the exterior of the solid. Hence, a minimum of two solid points is required for the solid to have a finite size; further, three fluid points at each side are used to define the cubic spline. The ADR IBM is used to compute the derivatives (advection, diffusion) for the provisional velocity in the fractional step method, which is not divergence free. Next, the Poisson equation

$$\Delta \pi = \nabla \cdot \{ [1 - \epsilon(x_i)] f_{\pi} \}, \quad (2.9)$$

is solved for π on the staggered grid where no reconstruction is applied when calculating the pressure forcing ∇f_{π} . The continuity equation in the presence of the IBM is now

$[1 - \epsilon(x_i)]\partial u_i/\partial x_i = 0$ and the Dirichlet boundary conditions of the velocity fields are $[1 - \epsilon(x_i)]u_i(x_i) = 0$. In addition, the ADR IBM is also implemented for a passive scalar, with the following boundary conditions $s(x_i) = [1 - \epsilon(x_i)]s(x_i) + s_{BCs}\epsilon(x_i)$, where s_{BCs} describes the fixed boundary values of the scalar. Here, the reconstruction is used for the derivatives in the advection and diffusion terms of (2.6a).

3. Surface roughness configuration

The targeted examination of small-scale roughness requires a small blocking ratio H/δ (Jiménez 2004), and is in contrast to urban-like geometries or other canopy flows where obstacles may cover a considerable portion of the boundary layer. This necessitates sufficient scale separation to yield values of H of the order of tens of wall units while keeping the blocking ratio limited below $\approx 1/100$. In comparison with simulations over aerodynamically smooth surfaces, the grid resolution needs consideration in all three directions: first, the viscous sublayer is not restricted to $z^+ \lesssim 5$ (Pope 2000) but forms around the obstacles, also on top of the elements such that we may expect a viscous sublayer up to $z^+ < H^+ + 5$. Second, the flow is also forced to rest at vertical walls, accompanied by sharp velocity gradients in the spanwise direction and an upward deflection in the streamwise direction. Hence, the horizontal grid must be sufficient for resolution of viscous sublayers at the vertical walls, which imposes additional constraints on the horizontal resolution.

We consider four simulations, one smooth and three rough cases with labels [s, r1, r2, r3]. The roughness properties are defined *a priori* in terms of the inner scaling of the smooth case (subscript $(\cdot)_s$), since the drag over the rough surface is unknown. The roughness consists of 56^2 elements of horizontally squared shape. The centroids of these elements are slightly displaced according to the roughness grid by up to ± 2 grid points in the horizontal directions, to break the symmetry (figure 3a). Heights and widths of the elements are uniformly distributed in the range of $\Delta H_s^+ \approx 10$ and $\Delta W_s^+ \approx 20$, that is $H_s \in [H_s^+ - \Delta H_s^+/2, H_s^+ + \Delta H_s^+/2]$ and similar for W_s , with mean heights of $H_s^+ = [9.9, 19.8, 29.5]$ and a uniform width of $W_s^+ = [39.8, 39.8, 39.9]$. The volume fraction covered by the roughness (A3d) at the ground is $\gamma^S = 1 - \gamma^F = 0.099$ and equals the plan area density $\lambda_p \hat{=} \gamma^S$. The frontal solidities of the three rough cases are $\lambda_f = [0.023, 0.047, 0.071]$. The surface area increases with respect to the horizontal L_{xy} -plane for the rough cases by $\Delta A_{eff} = 4\lambda_f$, since the roughness elements have a square base.

For consistency, we use the same computational grid and forcing parameters at $Re_D = 1000$ (note that simulation parameters are listed in table 1) for all four cases. The large-scale forcing is such that the mean velocity of the smooth case on the ground is approximately shear aligned, thus $\tau_{\star s} = \tau_{\star s, x}$. In the vertical, the grid spacing is $\Delta z_s^+ \approx 1$ up to the top of the roughness elements with $z_s^+ \geq 35$, where stretching begins. In the horizontal it is $[\Delta x_s^+, \Delta y_s^+] \approx 2.3$. Obstacles increase the drag, therefore the resolution in terms of wall units is expected to be coarser, which results in slight oscillations in velocities close to the roughness elements. Preliminary simulations showed that this effect is resolution dependent and is suppressed by a spectral cutoff filter at highest frequencies.

Interpolated turbulent fields from precursor simulations are used as initial conditions for the smooth simulation. In rotating systems, disturbances from the equilibrium state cause pervasive inertial oscillations with a period $2\pi/f$ (Appendix B, figure 17). We reduce those by replacing the mean in the three-dimensional velocity fields by a time and horizontal average over one inertial period. Once the smooth case has converged, we use velocity and passive scalar fields to initialize the rough simulations. The insertion of

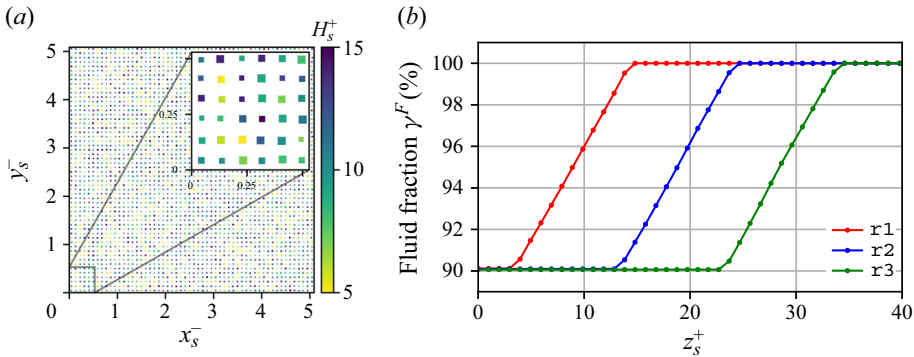


Figure 3. (a) Top view of the horizontal distribution of elements for case r1 and close-up view, colour coded according to their height; the horizontal axes are scaled by outer units of the smooth case. (b) Fluid fraction $\gamma^F(z_s^+)$ as a function of the distance from the wall for the rough cases r1, r2, r3 to illustrate the uniform height distribution of the elements; the vertical distance is scaled in smooth inner units. Round markers indicate the vertical position of grid nodes.

Re_A	Re_D	Sc	$N_{xy} \times N_z$	$(L_{xy} \times L_z)/\delta_s^3$	$\Delta x y_s^+ \times \Delta z_{s,min}^+$
5×10^5	10^3	1.0	$3072^2 \times 656$	$5.1^2 \times 4.9$	$2.3^2 \times 1.0$

Case	(ID)	H_s^+	W_s^+	ΔH_s^+	ΔW_s^+	λ_p [%]	λ_f [%]	ΔA_{eff} [%]
Rough	(r1)	10	40	10	20	10	2.3	9.2
Rough	(r2)	20	40	10	20	10	4.7	18.8
Rough	(r3)	30	40	10	20	10	7.1	28.4

Table 1. Upper table: grid, domain parameters and external Reynolds number for all cases presented in this study (subscript $(\cdot)_s$ relates to the smooth case), and the computational domain size normalized with the Rossby radius is $(L_{xy} \times L_z)/\Delta_{Ro}^3 = 0.27^2 \times 0.26$. Lower table: average height H_s^+ and width W_s^+ of the roughness elements for the rough cases, and their range of heights ΔH_s^+ and widths ΔW_s^+ . Also given are the plan area density λ_p , frontal solidity λ_f and the effective increase of the surface area ΔA_{eff} .

roughness elements in fully turbulent fields is possible since the numerical methods are stable and robust. Statistics of rough simulations are collected once the flow has adapted to the new boundary conditions. In eddy-turnover times, f^{-1} , flow statistics are collected for a timespan of [6.8, 2.3, 1.9, 6.3] (Appendix B); scalar statistics are considered over the final eddy-turnover time (§ 4.7).

The data used for statistical analyses in the remainder of this study are available for download at Kostelecky & Ansgore (2024) (<http://dx.doi.org/10.17169/refubium-43215>).

4. Results

4.1. Momentum budget and wall shear stress

For our configuration, roughness enhances the drag in comparison with smooth flow. However, the quantitative impact of our roughness arrangement (§ 3) on scalar and momentum transfer is unknown *a priori*. Total surface drag is the sum of pressure drag (also called ‘form’ drag), acting normal to the vertical walls of the cuboids, and of skin

friction drag, acting tangentially. The frictional drag may further be decomposed into ground-surface drag at $z = 0$ and roughness-element-surface drag (Shao & Yang 2008). The vertical component of the frictional drag on the roughness elements, the lift, is not of interest here.

Accurate quantification of horizontal drag exerted by roughness is essential for the subsequent analysis. A key feature of the Ekman flow is the veering of the wind with greater distance from the ground, due to the triadic balance of Coriolis, pressure gradient and frictional forces. This manifests in a non-zero spanwise component τ_{zy} such that

$$\langle \bar{\tau} \rangle(z) = \sqrt{\langle \bar{\tau} \rangle_{zx}^2 + \langle \bar{\tau} \rangle_{zy}^2}. \tag{4.1}$$

Over smooth surfaces, the wall shear stress $\tau_{*s} = \langle \bar{\tau} \rangle|_{z=0}$ reduces to the streamwise component $\tau_{*s} = \langle \bar{\tau} \rangle_{zx} \equiv 1/Re_\Lambda \partial \langle \bar{u} \rangle / \partial z|_{z=0}$, since we align the streamwise direction of the computational grid with τ_{*s} (§ 3 and figure 4, dashed lines). Over rough surfaces, we determine the total drag from the vertically integrated momentum equations (2.1b) in the streamwise and spanwise directions

$$\langle \bar{\tau} \rangle_{zi}(z) = \underbrace{- \int_0^z \frac{\partial \langle \bar{u} \rangle_i}{\partial t} dz}_T + \underbrace{+ f \int_0^z \epsilon_{ik3} (\langle \bar{u} \rangle_k - g_k) dz}_C + \underbrace{\frac{1}{Re_\Lambda} \frac{\partial \langle \bar{u} \rangle_i}{\partial z}}_V - \underbrace{\langle \overline{u'_i w'} \rangle}_R. \tag{4.2}$$

The total surface drag is composed of the temporal tendency (\mathcal{T}), Coriolis (\mathcal{C}), viscous (\mathcal{V}) and turbulent stress contributions (\mathcal{R}) (figure 4). Here, we define the turbulent contribution as the sum of turbulent (Reynolds) and dispersive stresses, since we study small-scale roughness.

The integrated temporal tendency is a measure of the convergence of a simulation towards its statistically steady equilibrium, and indeed cases s and $r3$ appear as statistically converged ($\partial_t(\cdot)/\partial t \approx 0$). For the rough cases $r1, r2$, we observe that they have not fully converged towards equilibrium in the outer layer, whereas in the near-wall region $z^+ < 300$ the integrated tendency is negligible. This behaviour is attributed to the different averaging times of the cases (Appendix B). Disturbances from the ground, i.e. the introduction of roughness elements into the flow, slowly progress to the outer layer, starting at $z^- \gtrsim 0.12$ and the relatively slower process of equilibration in the outer layer is apparently not converged after approximately 2–3 eddy-turnover periods.

Viscous friction dominates the momentum budget close to the wall (figure 4a), where the largest velocity gradient for the smooth case appears at $z = 0$, followed by a rapid decrease. With increasing roughness height a second peak develops for the cases $r2, r3$, linked to large velocity gradients at the top of the roughness elements. The turbulent stress dominates in the near-wall region away from the wall, with a maximum located above the roughness elements and a share of up to 80%. Turbulent stress increases with the roughness height in absolute values, pointing to enhanced turbulent mixing. The contribution of the Coriolis term is non-negligible within the roughness layer. At the top of the elements its contribution reaches up to 10%. With increasing roughness height, the veering of the wind inside the roughness layer is enhanced, underpinning the importance of the term \mathcal{C} to close the momentum budget in the roughness sublayer. Above the boundary-layer height, (4.2) is a balance between the Coriolis term, the total friction term, and for the non-converged cases the temporal tendency term.

The total surface drag of the smooth case is $\tau_{*s} = 2.82 \times 10^{-3}$, as estimated from the velocity gradient at $z = 0$. For the rough cases, τ reaches its maximum at the crest height of the highest elements, and it is $\|\tau_*\| = [3.36, 4.39, 5.38] \times 10^{-3}$.

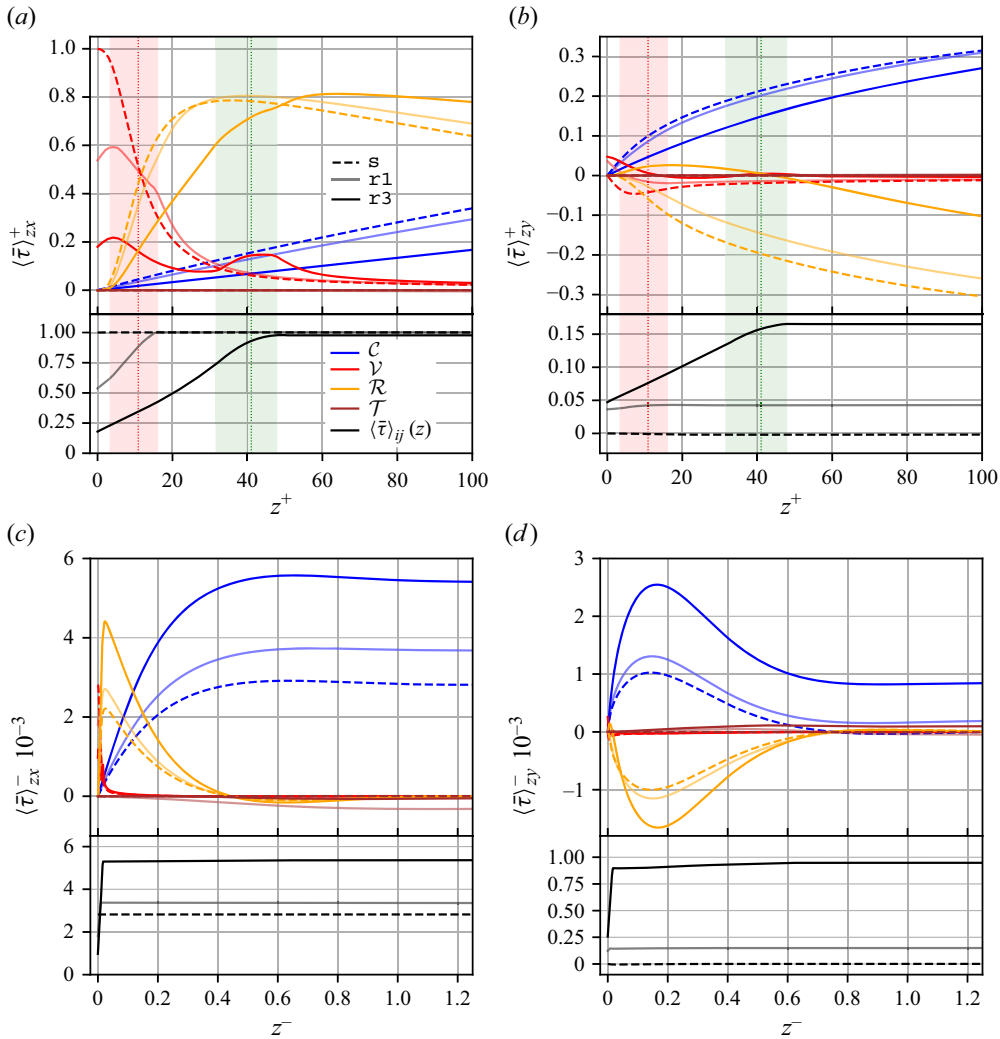


Figure 4. Integration of the mean momentum conservation in the streamwise (*a,c*) and spanwise directions (*b,d*), the terms according to (4.2). For clarity case r_2 is not shown and the total drag $\langle \bar{\tau} \rangle_{zj}(z)$ is moved to the lower panels of the plots. Colour shaded areas in the near-wall region in (*a,b*) correspond to the range of top heights of the roughness elements (cf. colour coding figure 3*b*), mean heights are displayed by vertical dotted lines. Shear stress components of the cases in the near-wall region (*a,b*) are scaled with the respective $1/u_{\star}^2$ and in the outer region in (*c,d*) with $10^{-3}/G^2$.

This gives a relative increase of the drag with respect to the smooth case of $\Delta_{rel} \|\tau_{\star}\| = [19.1\%, 55.7\%, 90.8\%]$; this corresponds to an increase of geostrophic drag of approximately 10%–40% (table 2). Notably, when the surface stress is determined from the values of the maximum turbulent stress in the constant-flux layer (where turbulent fluxes vary less than 10%, Stull 1988; Garratt 1992), approximately 20%–30% of the total stress is neglected (cf. figure 4*a*) for the configurations considered here. While this figure is likely on the upper end of expected outcomes for atmospheric conditions at higher Reynolds number, this illustrates that estimates of skin friction from inner-layer stress may experience considerable bias over rough surfaces.

Case (ID)	Smooth (s)	Rough (r1)	Rough (r2)	Rough (r3)
H^+	—	10.8	24.7	40.8
u_\star	0.0531	0.0580	0.0663	0.0733
α_\star	18.6	22.3	28.4	33.2
δ_{95}/δ_\star	0.612	0.621	0.594	0.578
δ_{CF}^+	[39, 91, 52]	[42, 101, 59]	[51, 121, 70]	[65, 147, 82]
$Re_\tau = \delta^+$	1408	1680	2196	2688
$Re_t = \max_z \{ \frac{e^2}{\nu \epsilon} \}$	764	895	1049	1254
$Re_k = \frac{\sqrt{K}\delta}{\nu}$	316	389	528	676

Table 2. Integral flow properties of the cases. The boundary-layer thickness δ_{95} refers to the height, where the total vertical flux is $\sqrt{\langle u'w' \rangle^2 + \langle v'w' \rangle^2} = 0.05u_\star^2$. The constant-flux layer δ_{CF}^+ refers to the layer between the maximum of the total vertical flux and the height where it is reduced by 10% of the maximum, and given as [start, end, extend] in inner units. The maximum for the Reynolds number of isotropic turbulence Re_t (defined in Ansgore & Mellado 2014, table 2, equation 5b) is always located above the highest roughness elements, and the Reynolds number for turbulence intensity Re_k is defined according to Schäfer, Frohnapfel & Mellado (2022a), where $K = \int_0^\delta e \, dz$ is the integrated TKE $e \equiv 0.5\langle u_i' u_i' \rangle$ within the boundary layer.

4.2. Scalar budget and scalar wall stress

The scalar flux is determined by the vertical integration of the scalar budget (2.6a)

$$\overline{\langle q \rangle(z)} = - \underbrace{\int_0^z \frac{\partial \langle s \rangle}{\partial t} \, dz}_{\mathcal{T}_s} + \underbrace{\frac{1}{Re_\Delta Sc} \frac{\partial \langle s \rangle}{\partial z}}_{\mathcal{V}_s} - \underbrace{\overline{\langle w' s' \rangle}}_{\mathcal{R}_s}, \tag{4.3}$$

with the temporal tendency \mathcal{T}_s , the viscous term \mathcal{V}_s and the scalar flux term \mathcal{R}_s (cf. their behaviour in figure 5), which incorporates again the Reynolds and dispersive stresses. Unlike the momentum budget, the passive scalar concentration in the boundary layer evolves in time. Hence, the vertical integration (4.3) precedes time averaging. Near the wall, again the tendency \mathcal{T}_s is small and the viscous contribution is relevant. For increasing roughness, the viscous stress is smeared out over the height of the roughness sublayer and a second peak similar to the one discussed for the momentum budget forms. This second peak becomes more dominant for increasing roughness and will eventually govern the viscous stress for large roughness elements or skimming flow. While the share of the turbulent contribution \mathcal{R} was limited to $\approx 80\%$ for momentum, mixing of the scalar is by far turbulence dominated, with a share of $\gtrsim 90\%$. In the outer region, the balance – in the absence of a rotational term – is governed by the turbulent scalar flux \mathcal{R}_s and the integrated tendency \mathcal{T}_s .

The surface flux of the scalar $q_{\star s}$ is estimated for the smooth case at $z = 0$ and for the rough cases, q reaches its maximum and at the same time constant value at the height of the highest elements, where q_\star is estimated. If temporal averaging of (4.3) is omitted, the development of $q_\star(t)$ and the friction of the scalar $s_\star(t) = q_\star(t)/u_\star(t)$ with the respective friction velocity $u_\star(t)$ are estimated (§ 4.7 and figure 14).

4.3. Global flow properties

The most prominent features when the turbulent flow is exposed to a rough surface are an increase in turbulence production associated with increased bulk shear stress $\|\boldsymbol{\tau}_\star\|$, a deeper boundary layer and higher turbulent Reynolds numbers (table 2). As $\delta^+ = Re_\tau$

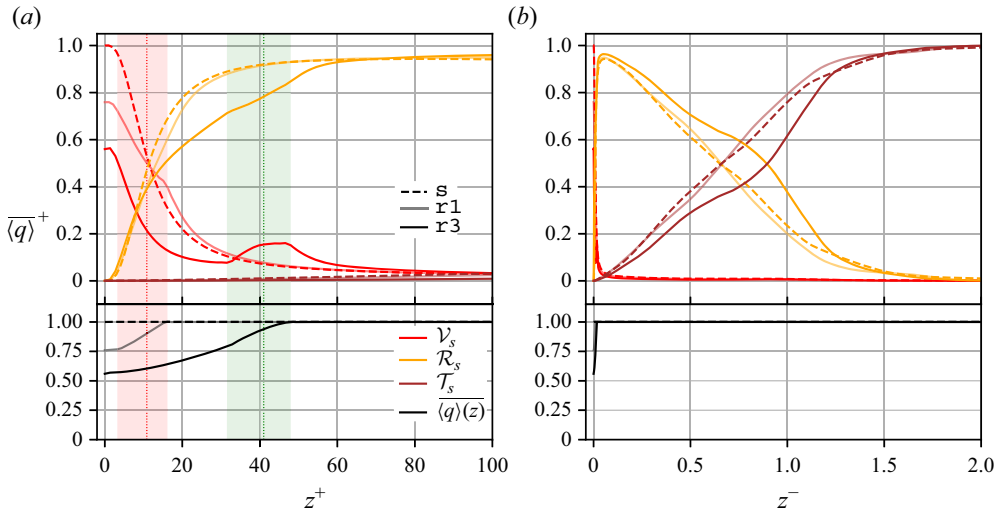


Figure 5. Integration of the mean passive scalar conservation (4.3). For clarity $r2$ is not shown and the scalar flux $\overline{\langle q \rangle}(z)$ is moved to the lower panels of the plots. (a) Terms in the near-wall region and (b) terms in the outer region are scaled with the respective $1/q_*$ and temporal averaging over the final eddy-turnover time (cf. colour coding and shaded areas in figure 4).

and $\|\tau_\star\|$ are linearly related, also Re_τ grows by up to 91 % (for the case $r3$). For the range of blocking ratios considered here, Re_τ appears to be a linear function of the height of the roughness elements; with $Re_D = \text{const.} = 1000$, this implies $u_\star \propto (H^+)^{1/2}$. As a consequence of increased u_\star , the grid resolution of case $r3$ in wall units is $\Delta xy^+ \times \Delta z_{min}^+ = 3.2^2 \times 1.4$ (compared with $2.3^2 \times 1.0$ for the smooth case). In inviscid units, i.e. normalized with Λ_{Ro} , the boundary-layer thickness $\delta_\Lambda = u_\tau / (f \Lambda_{Ro})$ also increases with H^+ (not shown in table 2). This illustrates an enhanced level of turbulence in the rough cases, quantifiable by an increase of Re_t and Re_k (table 2). Changes in global flow properties of case $r1$ are comparatively small, underpinning that the set-up is close to the aerodynamically smooth case s .

4.4. Wind veer in the surface layer

Due to surface friction, the wind veers in favour of the pressure gradient force as it approaches the surface (figure 6), giving rise to the Ekman spiral. While α_\star , the veer of the near-surface wind with respect to the outer layer is commonly taken into account by a rotation of the reference frame for surface-layer similarity (Ansorge 2019), wind veer within the atmospheric surface (Prandtl) layer, is commonly neglected (Monin 1970). Under this neglect, the surface layer becomes a componentwise ‘constant’-flux layer, i.e. the total vertical turbulent flux and its partitioning to the components is constant with height (commonly, a deviation of less than 10 % from the maximum value, usually measured close to the ground, is accepted). For the rough cases, the position of the constant-flux layer shifts upwards with H^+ , and it grows in extent when measured in inner units. Consistently with the increased scale separation, manifest in larger Re_τ , Re_k and Re_t , the constant-flux layer’s thickness increases both when expressed relative to Λ_{Ro} and when expressed in wall units by approximately 15 %.

Within the roughness sublayer, the direct effect of surface friction is strong, and we observe a veer of up to approximately 33° for case $r3$, nearly twice the veer of the smooth

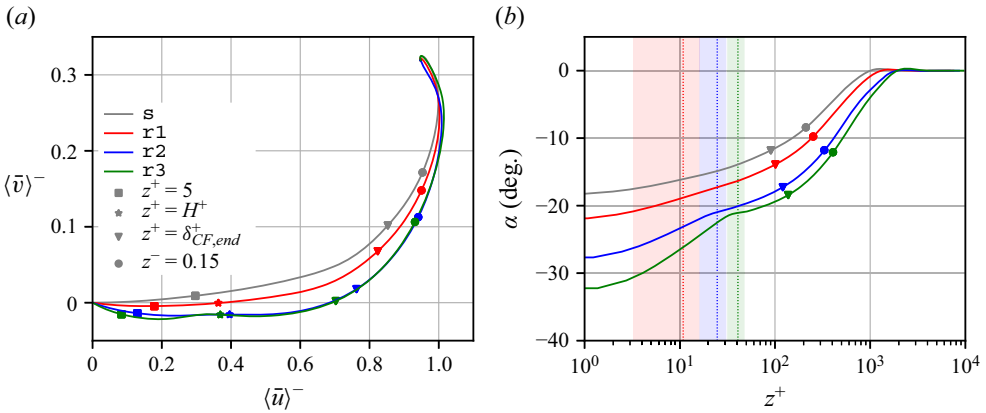


Figure 6. (a) Hodograph and (b) veering of the wind shown by means of the turning angle α (2.4a) of the surface shear stress to the geostrophic wind. Symbols in panel (b) correspond to the heights as labelled in panel (a), i.e. the end of the constant-flux layer as defined by a 10 % stress reduction and the upper bound of the inner layer $z^- = 0.15$ are marked.

case (18°). Close to the ground, for $z^+ < H^+$, both streamwise and spanwise velocity are slower compared with the smooth case (figure 6a), but the reduction of streamwise velocity is relatively stronger – manifest in the increased veer. In reach of the roughness tops, the turning angle α stays constant for r3, visible in the kink of the green curve in figure 6(b), which occurs for cases r2 and r3. As a consequence of the different wind veers within the surface roughness, the roughness field is approached at different angles for the cases presented here.

We find here that wind veer within the surface layer is not negligible for the current rough cases – and this effect appears to become stronger with increasing roughness. From previous studies on smooth Ekman flow and scaling arguments (Rossby & Montgomery 1935; Coleman *et al.* 1990), it is known that u_\star and α_\star decrease with higher Re (Shingai & Kawamura 2004) and increases for stably stratified conditions (Ansorge & Mellado 2014). Roughness, which acts to increase the scale separation in terms of Re_τ counteracts this relation by an increase in u_\star and α_\star ; that means, the dependence of α on the Reynolds number is outweighed by a stronger coupling of the outer and inner layers in the case of a rough surface such that overall the veering decreases. Roughness apparently comes into play as another important factor in real-world conditions for the strong dependence of both α and u_\star on the height of the roughness elements (figure 6). In fact, our simulations suggest that the dependence of wind veer on both roughness and surface friction is stronger than the effects of intermediate Reynolds number (a change of u_\star and α by 50 % due to variation of the Reynolds number requires a change of Re by several orders of magnitude while we have only varied the roughness height by approximately a factor three).

4.5. Aerodynamic parameters of the momentum

For the subsequent estimation of aerodynamic parameters, we use the total magnitude of the horizontal wind, defined as

$$\langle \bar{u}_h \rangle^+ = \sqrt{(\langle \bar{u} \rangle^+)^2 + (\langle \bar{v} \rangle^+)^2}. \tag{4.4}$$

This choice is in accordance both with atmospheric observations, where the wind magnitude is measured at different heights, and with previous numerical studies of Ekman

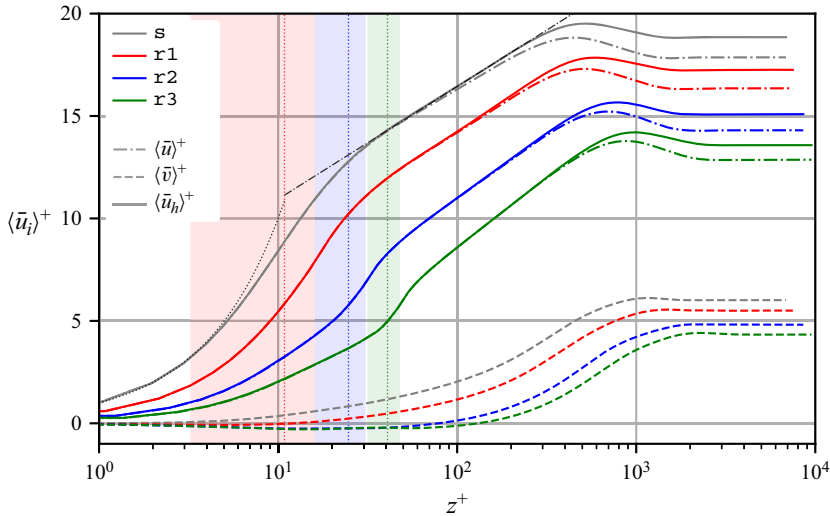


Figure 7. Intrinsically averaged velocity profiles in inner units. Displayed are the mean streamwise ($\langle \bar{u} \rangle^+$, dash-dotted lines), spanwise ($\langle \bar{v} \rangle^+$, dashed lines) and total horizontal velocity magnitudes ($\langle \bar{u}_h \rangle^+$, solid lines). For reference, the logarithmic and viscous laws are shown for the smooth case by thin dash-dotted and dotted lines, respectively. Parameters of the smooth logarithmic law are $\kappa_m = 0.42$, $A = 5.44$.

flow (Shingai & Kawamura 2004; Deusebio *et al.* 2014; Jiang, Wang & Sullivan 2018). For reference, we commence by consideration of the mean velocity profile for the smooth case s (figure 7) in inner and outer units. This profile agrees well with previous work (Spalart *et al.* 2008, 2009; Ansorge & Mellado 2014; Ansorge 2019): in the vicinity of the ground ($0 < z^+ \lesssim 5$), the viscous sublayer has a linear velocity profile $\langle \bar{u}_h \rangle^+ = z^+$. Above the viscous sublayer and the adjacent buffer layer, where turbulent production peaks, the logarithmic layer is found (Von Kármán 1930; Prandtl 1961; Zanon, Durst & Nagib 2003)

$$\frac{\partial \langle \bar{u}_h \rangle^+}{\partial z^+} = \frac{1}{\kappa_m z^+} \quad \text{or in the integrated form} \quad \langle \bar{u}_h \rangle^+ = \frac{1}{\kappa_m} \ln(z^+) + A. \quad (4.5a,b)$$

Here, κ_m is the von Kármán constant and A an integration constant encoding the lower boundary condition, i.e. the integrated velocity profile of the viscous and buffer layers. The exact vertical bounds of the logarithmic layer are a matter of debate; following Marusic *et al.* (2013), the logarithmic region for the streamwise turbulent intensity is located at $3\sqrt{Re_\tau} < z^+ < 0.15Re_\tau$. For the smooth case, we choose $z^+ > 30$ as a common value for the lower boundary (Tennekes & Lumley 1972) and $z^+ < 0.15Re_\tau$ as the upper boundary. Within this region, we estimate $\kappa_m = 0.42$ and $A = 5.44$ from a least squares fit.

Over rough surfaces, the logarithmic law is expressed as

$$\langle \bar{u}_h \rangle^+ = \frac{1}{\kappa_m} \ln(z - d_m)^+ + A - \Delta \langle \bar{u}_h \rangle^+ = \frac{1}{\kappa_m} \ln\left(\frac{z - d_m}{z_{0m}}\right), \quad (4.6)$$

where d_m is the zero-plane displacement height, a function of the packing density of roughness elements (Placidi & Ganapathisubramani 2015), and $\Delta \langle \bar{u}_h \rangle^+ = A + \kappa_m^{-1} \ln(z_{0m}^+)$ is the roughness function (Clauser 1954; Hama 1954), which describes the additional momentum loss due to roughness. Also, A is an integration constant. The roughness function measures the deceleration of the velocity with respect to smooth flow within the logarithmic region (figure 8a). If the surface is smooth, the parameters

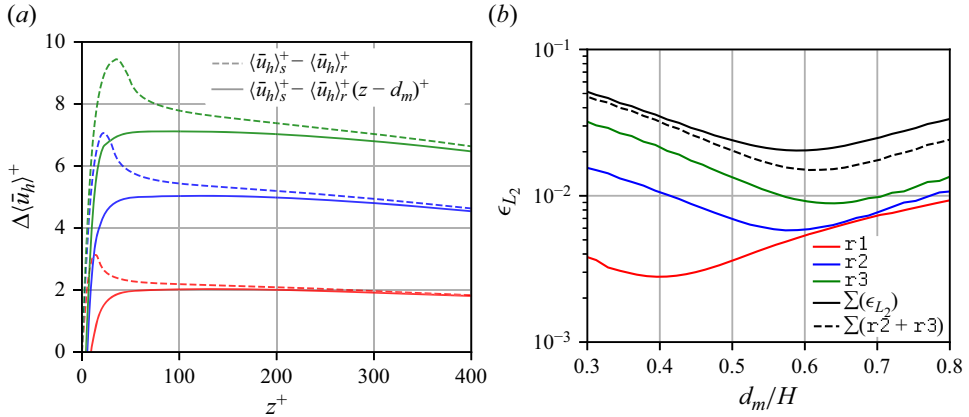


Figure 8. (a) Roughness function for the horizontal velocity magnitude. (b) Relative error ϵ_{L_2} of the present velocity profiles and the logarithmic law fit for an optimal z_{0m} as a function of the normalized displacement height d_m/H .

d_m , $\Delta\langle\bar{u}_h\rangle^+$ are zero. The aerodynamic roughness length z_{0m} for the smooth case is $z_{0m}^+ = e^{-\kappa_m A} \approx 0.1$. Traditionally, the equivalent sand-grain roughness Reynolds number $k_s^+ = k_s u_* / \nu$ is used to compare different roughness set-ups. The roughness function follows, in the fully rough regime, a logarithmic law $\Delta\langle\bar{u}_h\rangle^+ = \kappa_m^{-1} \ln(k_s^+) + A - A'_{FR}$ (cf. equation 2.2 in Squire *et al.* 2016). With the constant $A'_{FR} = 8.5$ (Nikuradse 1933) the relation $k_s^+ \approx 35.5 z_{0m}^+$ directly appears and is valid under fully rough conditions. Both forms of the rough log law (4.6) are interchangeable, whereas the first expression is preferably used in an engineering context and the second in a meteorological context.

In the quest for a universal scaling for the mean velocity profiles in the logarithmic region, an optimization problem over the set of parameters $\{\kappa_m, z_{0m}, d_m\}$ arises, which is challenging to solve. Therefore, the following assumptions are drawn. First, the von Kármán constant is universal in this study, since the only difference in the simulation set-ups of the cases are in the surface conditions. The observed dependence of the von Kármán constant on the roughness Reynolds number $\kappa_m = f(z_0^+)$ in atmospheric measurement data in the fully rough regime (Frenzen & Vogel 1995a,b) is according to Andreas *et al.* (2006) an artificial consequence of correlation when calculating the parameters. We follow the notion of κ_m as a universal constant for canonical flows over smooth (Nagib & Chauhan 2008) and rough surfaces (Castro & Leonardi 2010). As shown below, the roughness Reynolds number varies by approximately one decade in the current cases. The increase of roughness heights among cases r1–r3 is considered via an adjusted fitting interval for the logarithmic law (4.6). That is, second, we assume the logarithmic layer is located in the range $z_{log,m}^+ < z^+ < 0.15 Re_\tau$, where we use $z_{log,m}^+ = 30 + d_m^+$. (Due to the small value of H , the choice of $z_{log,m}^+$ fits the data, and should not be interpreted as predictive or general; great care should be taken with respect to higher-order statistics.) The subsequent analysis shows that we are still well within the logarithmic range of the flow with the choice of the lower limit $z_{log,m}^+$. Third, the normalized displacement height d_m/H is assumed to be constant for all rough cases. In fact, this ratio is known to be mainly governed by the roughness density λ_p and an unclear relation of λ_f for $\lambda_f < 0.1$ (Placidi & Ganapathisubramani 2015, figure 11).

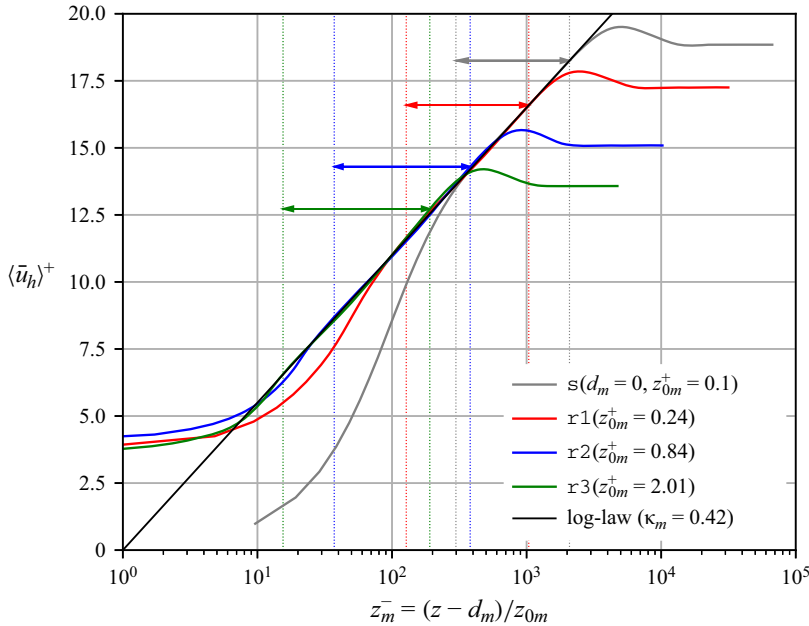


Figure 9. Collapse of the mean horizontal velocity profiles onto the logarithmic law of the wall, with the zero-plane displacement height $d_m/H = 0.59$. Coloured arrows and vertical dotted lines indicate the fitting interval for the logarithmic law of each case.

To determine the optimal value of d_m/H , an error norm ϵ_{L_2} is defined for each of the corresponding intervals in (figure 8b)

$$\epsilon_{L_2}(\langle \bar{u}_h \rangle^+) |_{d_m, z_{0m}} = \frac{1}{n} \sqrt{\sum_{i \in \{z^+ | z_{\log, m}^+ < z^+ < 0.15 Re_\tau\}}^n \left[\langle \bar{u}_h \rangle_i^+ - \frac{1}{\kappa_m} \ln \left(\frac{z_i - d_m}{z_{0m}} \right) \right]^2}. \quad (4.7)$$

The optimum value of d_m/H minimizes the expression $\{\sum_{k \in \{r1, r2, r3\}} \epsilon_{L_2}\}$. We find the optimal value of $d_m/H \approx 0.59$ (cf. black curve in figure 8b) in accordance with literature data for $\lambda_p = 0.1$ (Kanda *et al.* (2004) with LESs over cube roughness $d_m/H \approx 0.65$, Leonardi & Castro (2010) with DNS over staggered cube roughness with $d_m/H \approx 0.6$ and Brutsaert (1982) for crop covered surfaces $d_m/H \approx 2/3$). Excluding case r1 (which is almost aerodynamically smooth) from the sum would result in a negligible change of the optimal value of $d_m/H \approx 0.61$.

The mean velocity profiles collapse onto the proposed rough log law (4.6) when scaled with u_\star and the vertical distance with $z_m^- = (z - d_m)/z_{0m}$ (figure 9). We obtain values of the normalized aerodynamic roughness length of $z_{0m}/H = [0.022, 0.034, 0.049]$ and scaled in inner units $z_{0m}^+ = Re_{z_{0m}} = [0.24, 0.84, 2.01]$. In the ABL, the onset of the fully rough regime is assumed for $z_{0m}^+ \gtrsim 2-2.5$, and the transitionally rough regime for $0.135 \lesssim z_{0m}^+ \lesssim 2-2.5$ (Brutsaert 1982; Andreas 1987). By this definition, cases r1, r2 are transitionally rough and r3 is on the edge of being fully rough when considered in terms of z_{0m}^+ . Taking into account that the transition between roughness regimes is highly dependent on the type of roughness, we conclude that case r3 is fully rough for (i) its sharp-edged geometry, (ii) the occurrence of a dual peak in the viscous stress and (iii) the strong signature of roughness in all turbulent statistics. Figure 9 illustrates that the increase

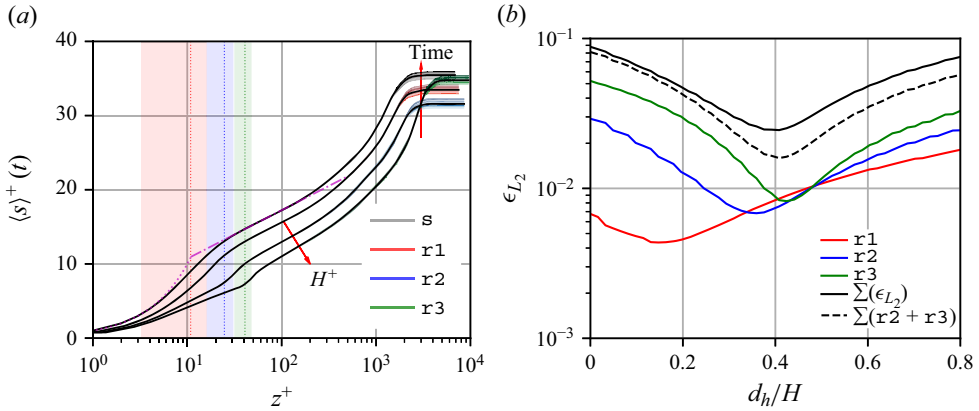


Figure 10. (a) Temporal evolution of the horizontally averaged scalar profile in inner units, shown together with the temporal mean (solid black lines). The viscous law (magenta dotted line) with $\langle \bar{s} \rangle^+ = z^+ Sc$ and the logarithmic law (magenta dashed-dotted line) $\langle \bar{s} \rangle^+ = \kappa_h^{-1} \ln(z^+) + \mathbb{A}$ with $\kappa_h = 0.35$, $\mathbb{A} = 4.2$ are shown for case s. (b) Relative error ϵ_{L_2} of the present scalar profiles and the logarithmic law fit for an optimal z_{0h} as a function of the normalized displacement height d_h/H .

of Re_τ for the rough cases also manifests in a deeper logarithmic layer, i.e. the common bounds of the logarithmic region also hold over the rough surface. In fact, the previous lower limit of $z^+ > z_{\log,m}^+$ can be adjusted downward to $z^+ > 25 + d_m^+$ or to $z^+ > 0.8\sqrt{Re_\tau}$ as a function of the Reynolds number, without z_{0m}^+ differing by more than $\pm 5\%$ from the above values. The proposed procedure of estimating the aerodynamic properties of the flow is robust to the choice of the displacement height, since changing $d_m/H = 0.6 \pm 0.1$ results in maximum deviation of the presented z_{0m}^+ values of $\pm 4.5\%$ (cf. small variation of ϵ_{L_2} vs d_m/H in figure 8b).

4.6. Aerodynamic parameters of the passive scalar

Despite the temporal evolution of mean scalar profiles $\langle s \rangle^-$ (figure 10a), $\langle \bar{s} \rangle^+$ is statistically steady in the logarithmic layer: the inner layer is in quasi-equilibrium with the scalar evolution in the outer layer. In the immediate vicinity of a smooth wall (case s) we resolve the conductive sublayer with $\langle \bar{s} \rangle^+ = z^+ Sc$. In analogy with the momentum logarithmic layer (4.6), the scalar one reads as

$$\langle \bar{s} \rangle^+ = \frac{1}{\kappa_h} \ln(z - d_h)^+ + \mathbb{A}(Sc) - \Delta \langle \bar{s} \rangle^+ = \frac{1}{\kappa_h} \ln\left(\frac{z - d_h}{z_{0h}}\right), \quad (4.8)$$

where κ_h is the von Kármán (Sc) constant and the constant of integration $\mathbb{A}(Sc)$ encodes the surface information. For (aerodynamically) smooth surfaces, it is $d_h = 0$ and $\Delta \langle \bar{s} \rangle^+ = 0$; for rough surfaces, the displacement height $d_h > 0$, the roughness function $\Delta \langle \bar{s} \rangle^+ \neq 0$ and an aerodynamic roughness length z_{0h} emerges. We determine the parameters from our simulation data following the procedure described above and find the von Kármán constant $\kappa_h \approx 0.35$. While existing data of experiments appear to agree on $\kappa_h \approx 0.47$, DNS data yield a large spread in the range $0.28 \lesssim \kappa_h \lesssim 0.46$ (table 3). The experimental data available (table 3) do, however, not consider external flow while externality of the flow is known to impact estimates of κ and can explain a substantial share of the variation in κ from simulation data (Ansorge & Mellado 2016).

Reference	Type (BCs)	Re_τ	Sc	κ_h	$\mathbb{A}(Sc)$
Kader (1981)	exp. data (collection)	multiple	1.0	0.47	6.5
Subramanian & Antonia (1981)	exp. boundary layer	multiple	—	0.48 ± 0.02	2.0 ± 0.02
Kasagi, Tomita & Kuroda (1992)	DNS channel (v)	150	0.71	0.36	2.09
Kawamura, Abe & Matsuo (1999)	DNS channel (f)	180, 395	0.025–0.71	0.4–0.42	—
Johansson & Wikström (2000)	DNS channel (v)	265	0.71	0.33	0.95
Kawamura, Abe & Shingai (2000)	DNS channel (f/v)	180, 395	0.025–1.0	0.28 (v), 0.41 (f)	—
Pirozzoli, Bernardini & Orlandi (2016)	DNS channel	548–4088	0.2–1.0	0.46	—
Pirozzoli <i>et al.</i> (2022)	DNS pipe flow (v)	6000	1.00	0.459	5.78
Cases of this study (s, r1, r2, r3)	DNS Ekman flow (v)	1408–2688	1.00	0.35	4.2

Table 3. Parameters $\{\kappa_h, \mathbb{A}(Sc)\}$ for the logarithmic law of the passive scalar. If known, boundary conditions (BCs) for the scalar are indicated with (v) for constant value or (f) for constant flux. All DNS of turbulent channel flow are closed channels. Kader (1981) gives a function for the integration constant with $\mathbb{A}(Sc) = (3.85Sc^{1/3} - 1.3)^2 + 2.12 \ln Sc$.

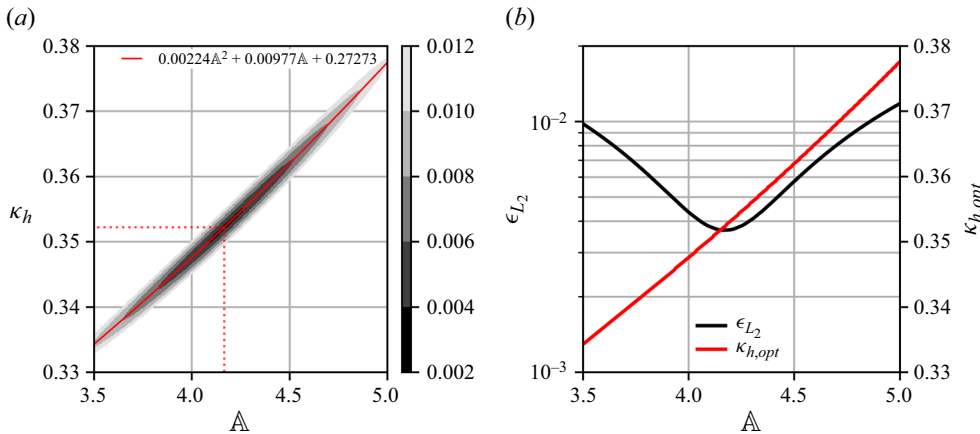


Figure 11. (a) Shading of the error norm ϵ_{L_2} (according to (4.7)) for the least squares fit of $\{\kappa_h, \mathbb{A}\}$ of the passive scalar of the smooth case s. The red line indicates a polynomial fit to the minimum error norm and the best fit is marked with red dotted lines. (b) The error norm ϵ_{L_2} as a function of \mathbb{A} for an optimal value of κ_h, opt in black and $\kappa_{h, opt}$ as function of \mathbb{A} in red.

The constants κ_m and A of the logarithmic law for the mean velocity are known to be strongly correlated for the momentum log law (4.5; Anson & Mellado 2016; Anson 2017), which also holds for the scalar and is quantified in figure 11(a). For the smooth case s, the rather flat curve of the error norm ϵ_{L_2} (evaluated similar to (4.7)) for the scalar allows values of the von Kármán constant κ_h in the range of $0.34 \lesssim \kappa_h \lesssim 0.37$ (figure 11b). For the rough cases, we again pose universality of $\kappa_h = 0.35$ and minimize the error norm analogous to (4.7), which is shown in figure 10(b), to estimate the scalar displacement

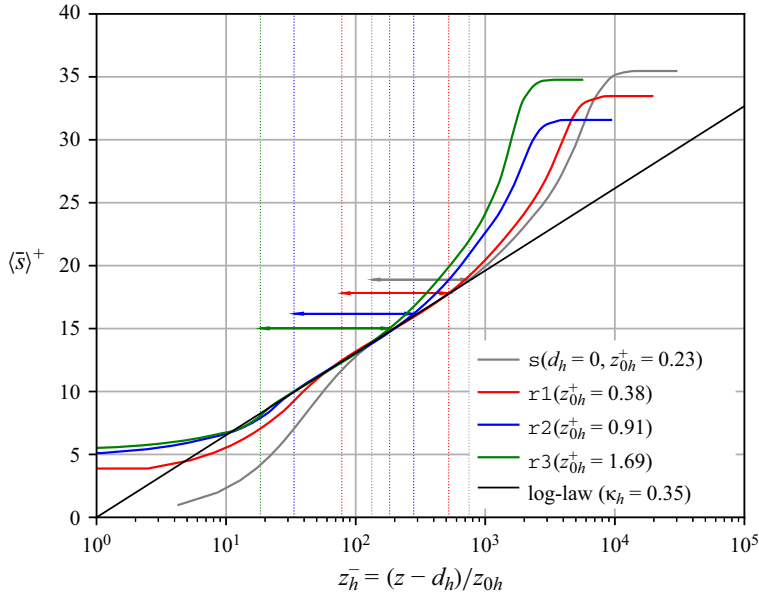


Figure 12. Collapse of the mean scalar profiles onto the logarithmic law of the wall, with the zero-plane displacement height $d_h/H = 0.41$. Coloured arrows and vertical dotted lines indicate the fitting interval for the logarithmic law of each case.

height $(d_h/H)_{opt} = 0.41$ for all rough cases; as expected, this height is substantially lower than that of the momentum, which illustrates the absence of pressure-blocking effects for the scalar exchange in comparison with momentum exchange.

The collapse of profiles to the proposed logarithmic law is shown in figure 12 with $z_{log,h}^+ < z^+ < 0.12Re_\tau$ for rough cases, where $z_{log,h}^+ = 30 + d_h^+$. (Due to the small value of H , the choice of $z_{log,h}^+$ fits the data, and should not be interpreted as predictive or general. Great care should be taken with respect to higher-order statistics.) For the smooth case, we find $z_{0h}^+ = e^{-\kappa_h \Delta} = 0.23$, more than twice the momentum roughness length z_{0m} . And for the rough cases, it is $z_{0h}/H = [0.035, 0.037, 0.040]$ or, in inner units, $z_{0h}^+ = [0.38, 0.91, 1.69]$. In contrast to the momentum roughness length z_{0m}/H , which increases by more than a factor two, the normalized scalar roughness length z_{0h}/H depends only weakly on the blocking ratio. This difference is due to the absence of pressure-blocking effects in the scalar budgets that hamper vertical momentum exchange in the viscous region.

4.7. Scaling behaviour of aerodynamic parameters

The z -nought concept with parameters z_{0m} , z_{0h} lumps the roughness effects for the near-surface transport of scalar and momentum (in addition to their displacement heights d_m and d_h commonly considered to be related to the covered volume only). These z -nought parameters are key for the modelling of surface momentum and scalar exchange (Monin 1970; Foken 2006). The mixing of momentum is determined by both pressure drag and viscous drag over rough surfaces, while scalar mixing lacks the pressure-blocking effect and is therefore described by molecular diffusion alone (Cebeci & Bradshaw 1984, p.168), as already discussed when determining z_{0h} (§ 4.6; cf. also Brutsaert 1982, § 5; Garratt 1992, § 4). In the ABL $z_{0m} > z_{0h}$, since mixing of momentum is more efficient than scalar

Small-scale roughness in Ekman flow

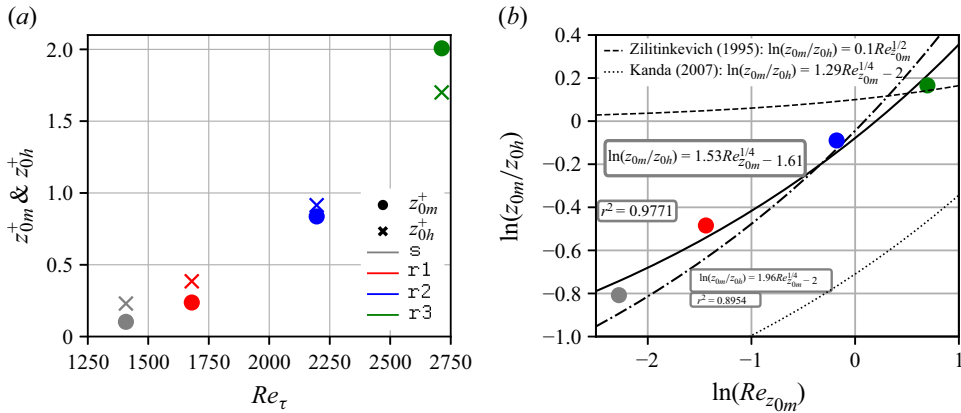


Figure 13. (a) Aerodynamic roughness lengths of momentum z_{0m}^+ and scalar z_{0h}^+ as a function of the friction Reynolds number. (b) Log ratio of the momentum and scalar roughness length plotted as a function of the logarithm of the roughness Reynolds number $\ln(Re_{z_{0m}})$, with exponential fitting functions (solid and dot-dashed black lines) and the corresponding values of r^2 (coefficient of determination). The dashed and dotted lines are according to Zilitinkevich (1995) and Kanda *et al.* (2007).

mixing due to pressure gradients in the roughness sublayer (cf. also LES studies with cubical roughness by Li & Bou-Zeid 2019 and Li *et al.* 2020).

Commonly, z_{0m} is determined as a site-specific parameter from wind profiles, with due regard of roughness geometry and arrangement. Different approaches exist to parametrize z_{0h} based on z_{0m} . Conventionally, $\ln(z_{0m}/z_{0h}) \propto Re_{z_{0m}}^n$ is assumed for constant Schmidt number. A review of classical theories is given by Li *et al.* (2017). Zilitinkevich (1995) proposed an exponent $n = 1/2$ and Brutsaert (1975a,b) an exponent of $n = 1/4$. For the roughest case r3 we observe the proposed behaviour of $z_{0m} > z_{0h}$ (figure 13a), which supports our assertion that case r3 is in between the transitionally and fully rough regimes, where pressure drag dominates. For the other cases, the scalar roughness length exceeds the aerodynamic one. Following the scalings of Brutsaert (1982) and Kanda *et al.* (2007), we estimate the scaling for the log ratio of roughness lengths as $\ln(z_{0m}/z_{0h}) = 1.96Re_{z_{0m}}^{1/4} - 2$, whereas the best fit collapses on $\ln(z_{0m}/z_{0h}) = 1.53Re_{z_{0m}}^{1/4} - 1.61$. An extrapolation to the fully rough regime $z_{0m}^+ > 2$ is, however, delicate due to the lack of data.

We observe a linear relation of u_\star as a function of the height of roughness elements expressed in external units Λ_{Ro} (figure 14a) in the transitionally rough regime. This scaling appears despite the change in wind direction with which the roughness field is approached for the cases (cf. figure 6b). The scaling behaviour of the friction values of the passive scalar is not as conclusive as for u_\star , since the scalar is evolving in time (figure 14b) and processes act on different time scales. The imposed initial state of the passive scalar adapts to the imposed boundary conditions on the shortest possible, namely the viscous, time scale (cf. near-sudden increase for the rough cases at $tf = 0$, and strong increase for the smooth case at $tf \approx -2.7$, figure 14b). Following this initial transition, the scalar gets mixed vertically across the boundary layer by turbulence at the turbulent time scale f^{-1} . If time is allowed to get sufficiently large, processes at the largest time scale $\propto Re_\Lambda$ become relevant. Here, the scalar is mixed by laminar diffusion between the top of the boundary layer and the top of the computational domain at a time scale ν/G^2 (here, $\sim Re_\Lambda$). This separation of time scales is indeed supported by the process of scalar mixing across the ABL (figure 15): after the initial transient, disturbances propagate upwards through the

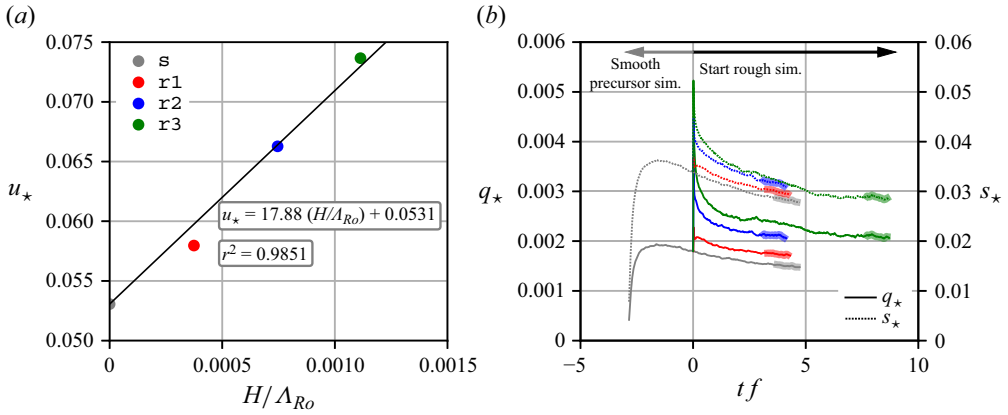


Figure 14. (a) Scaling of the friction velocity u_* as function of the mean height H/Λ_{Ro} of the roughness elements, normalized with the Rossby radius Λ_{Ro} . The linear function is derived by fitting the slope parameter, whereby the vertical offset parameter is equal to the value of the smooth case s . With the corresponding r^2 value of the linear fit. (b) Temporal evolution of the friction scalar $s_*(t)$ and the surface flux $q_*(t)$. Time is scaled with eddy-turnover times f^{-1} (cf. Appendix B for $u_*(t)$).

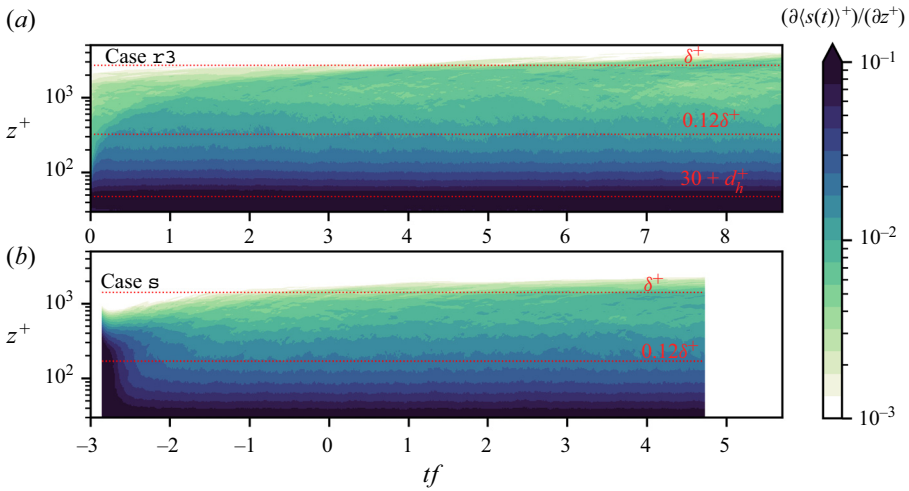


Figure 15. Temporal evolution of the horizontally averaged gradient of the passive scalar for (a) case $r3$ and (b) case s , scaled in inner units. The upper boundary of the logarithmic layer is indicated with $z^+ = 0.123\delta^+$, the lower boundary with $z^+ = z_{\log,h}^+$ ($d_h^+ = 0$ for case s) and the boundary-layer thickness with δ^+ . The lowest part $0 \leq z^+ < 30$ of the boundary layer is not shown.

logarithmic layer and above. Mixing in the upper part of the boundary layer is visible for case $r3$ (figure 15a) at time $tf \gtrsim 6.5$. This is also seen in figure 14(b) in terms of a decreased rate in q_* and u_* for $tf \gtrsim 6.5$. The less rough cases have not reached this quasi-steady regime, which points to enhanced turbulent mixing for the roughest case. Nevertheless, mean passive scalar statistics are sufficiently converged in the logarithmic layer so they have reached a quasi-equilibrium, and they are analysed for the period of the final eddy-turnover time of each case.

Based on figure 14(b), we find that the change of s_* with respect to H/Λ_{Ro} in equilibrium is small in comparison with the change of u_* . From the data available it is, however,

not clear whether s_\star becomes a constant or changes weakly with respect to H/Λ_{Ro} . The key difference between the conservation equations for momentum (2.1b) and passive scalar (2.6a) is the pressure gradient term $-\partial\pi/\partial x_i$. The friction velocity u_\star changes by up to 38% while the change of q_\star is largely explained by a change of u_\star such that s_\star remain approximately constants. This behaviour underlines the strong link between roughness effects on the momentum conservation and the pressure drag.

5. Discussion and conclusions

Direct numerical simulations of turbulent Ekman flow with a passive scalar are carried out for a rough surface resembling a typical ABL configuration over homogeneous roughness. The roughness is fully resolved and considered through an ADR IBM, which allows us to maintain a high order of spatial discretization while avoiding SFOs. The fully resolved small-scale roughness (blocking ratio H/δ of the order of $O(1\%)$) has the form of 56^2 rectangular blocks on the surface; these blocks feature a uniform height and width distribution. In total, four simulations with identical large-scale forcing are performed: one smooth case s at $Re_\tau = 1408$ and three rough cases $r1, r2, r3$ with increasing roughness heights $H^+ = [10.8, 24.7, 40.8]$. Regarding our research questions posed in § 1, we find the following:

- (i) For a controlled and fully resolved surface roughness, friction velocity u_\star and scalar s_\star can be determined by integration of the scalar and momentum budgets. The increase for u_\star is up to 38% and for Re_τ up to 91%. The results of the passive scalar indicate the importance of the pressure drag on the momentum, especially for the fully rough case $r3$, in which momentum transfer is dominated by pressure drag and scalar transfer by molecular diffusion (Cebeci & Bradshaw 1984, p. 168). With increasing roughness height the turbulent activity and therefore mixing is enhanced. The influence of roughness on the turning of the wind and hence the Ekman spiral manifests in an enhanced turning angle α . This is despite an increasing scale separation in viscous units, and it illustrates that, in terms of outer scaling, roughness acts to reduce the Reynolds number; i.e. the scale separation for large eddies is governed by Re_τ/Re_{z_0} rather than by Re_τ . This means that – from the perspective of large eddies – the ABL has a lower Reynolds number than is usually assumed by a factor Re_{z_0} .
- (ii) The DNS data collapse onto the rough-wall scaling in the logarithmic layer for the mean horizontal velocity and passive scalar. The estimated von Kármán constants and offset parameters are $\kappa_m = 0.42, A = 5.44$ and $\kappa_h = 0.35, \mathbb{A} = 4.2$. A strong correlation between the von Kármán constant κ and the offset parameter A is quantified. In the presence of roughness, the extent of the logarithmic layer in inner units grows with increasing roughness height and therefore scale separation. We, however, find that the commonly assumed representation of the total drag by the maximum of the turbulent drag in the lower part of the surface layer may constitute a substantial bias in rough boundary layers as a substantial fraction of up to 20% of the drag is neglected when considering the turbulent drag only. The substantial variation of drag in the inner layer (below $z^- \approx 0.15$) comes with rotational effects (due to the triadic balance between the Coriolis force, pressure gradient and viscous drag) in the roughness sublayer that manifest in a wind veer across the lowest part of the ABL, even below the logarithmic layer.
- (iii) Based on our data, we estimate the zero-plane displacement height for momentum to $d_m/H \approx 0.6$ and for the scalar to $d_h/H \approx 0.4$ and roughness Reynolds numbers

of $z_{0m}^+ = [0.1, 0.24, 0.84, 2.01]$ and $z_{0h}^+ = [0.23, 0.38, 0.91, 1.69]$. This leaves the cases $r1, r2$ in the transitionally rough regime and the roughest case $r3$ at the edge of the fully rough regime.

- (iv) The log ratios of the roughness lengths $\ln(z_{0m}/z_{0h})$ exhibit a clear scaling $\propto Re^{1/4}$, which fits the known exponent of Brutsaert (1975a,b). For the smooth and transitionally rough regime scalar mixing is enhanced $z_{0m} < z_{0h}$, whereas in the fully rough regime $z_{0m} > z_{0h}$ is recovered, due to the importance of the pressure.

With the framework prescribed in this study, we are now able to study the impact of roughness on the ABL at meaningful scale separations. The extension of these results to the fully rough regime for the scaling of aerodynamic parameters outside the transitionally rough regime as well as the effects of heterogeneous surface conditions on the stably stratified flow are interesting aspects for future work.

Acknowledgements. We are grateful for the comments of the anonymous reviewers who helped shape this article. Simulations were performed on the resources of the High-Performance Computing Center Stuttgart (HLRS) on the Hawk cluster, founded by the Baden–Württemberg Ministry for Science, Research, and the Arts and the German Federal Ministry of Education and Research through the Gauss Centre for Supercomputing. The computing time and storage facilities were provided by the project trainABL with the project number 44187.

Funding. The authors acknowledge financial support through the ERC grant trainABL with the project number 851374; DOI: <https://doi.org/10.3030/851374>.

Declaration of interests. The authors report no conflict of interest.

Data availability statement. The data supporting the findings of this study are published in Kostelecky & Ansonge (2024).

Author ORCIDs.

Jonathan Kostelecky <https://orcid.org/0000-0002-9983-9310>;

Cedrick Ansonge <https://orcid.org/0000-0001-9913-3759>.

Author contributions. J.K. performed the code implementation, carried out the numerical simulations, performed the post-processing of the data, worked on visualization and interpretation of results and wrote the original draft. Both authors contributed to the conceptualization of the study. C.A. supervised the research, contributed with discussion and interpretation of results, reviewed and edited the original draft and was responsible for acquisition of funding.

Appendix A. Intrinsic averaging in an inhomogeneous domain

Let us consider a square object immersed in a fluid domain (cf. figure 2a, red shaded area), which covers a normalized solid area of $A^1 = 4$ and fluid area of $A^0 = 21$ and $N^1 = 9$, $N^0 = 16$ grid points (superscripts $(\cdot)^{0,1}$ are used according to (2.8)). The mean of any flow variable φ_i in the solid and fluid region is defined as follows:

$$\langle \varphi_i \rangle^0 = \frac{1}{N^0} \sum_{i \in A^0} \varphi_i, \quad \text{and} \quad \langle \varphi_i \rangle^1 = \frac{1}{N^1} \sum_{i \in A^1} \varphi_i. \tag{A1a,b}$$

Evidently, this approach neglects contributions to the fluid, because of the mismatch in $A^0/(A^0 + A^1) \neq N^0/(N^0 + N^1)$ (red, blue shaded area), therefore a volume-based approach (for the three-dimensional case) is needed to take precisely the covered space into account. Depending on the location of a certain grid point, the distinction between solid and fluid is augmented by grid points on corners, edges and plane interfaces (cf. figure 2b)

with

$$\epsilon^S(x_j) = \begin{cases} 1, & \text{if } x_i \in \text{fluid,} \\ \frac{1}{2}, & \text{if } x_i \in \text{plane interface,} \\ \frac{1}{4}, & \text{if } x_i \in \text{edge,} \\ \frac{1}{8}, & \text{if } x_i \in \text{corner,} \\ 0, & \text{if } x_i \in \text{solid,} \end{cases} \quad \text{and } \epsilon^F(x_i) = [1 - \epsilon^S(x_i)]. \quad (\text{A2a,b})$$

Expanding the approach to the three-dimensional case leads to height-dependent volume fractions

$$\gamma^0(z) = \langle 1 - \epsilon(x_i) \rangle, \quad \gamma^F(z) = \langle 1 - \epsilon^S(x_i) \rangle, \quad (\text{A3a,b})$$

$$\gamma^1(z) = 1 - \gamma^0(z), \quad \gamma^S(z) = 1 - \gamma^F(z), \quad (\text{A3c,d})$$

$$\gamma^{rel}(z) = \frac{\gamma^0(z)}{\gamma^1(z)}, \quad (\text{A3e})$$

which are easily validated by $\gamma^F(z) - \gamma^0(z) = \gamma^1(z) - \gamma^S(z)$. We are interested in the mean conditional statistical moments in the fluid region, since any statistics inside the solid regions are irrelevant. The statistical output of the DNS code provides only the unconditional mean $\langle \varphi_i \rangle^{code}$ and (co-)variances $\langle \varphi'_i \varphi'_j \rangle^{code}$ of the flow variables. Following the conditional averaging approach in Pope (2000, p. 169f), the mean can be easily conditioned to the fluid region with

$$\langle \varphi \rangle_i^F = \frac{1}{\gamma^F} (\langle \varphi_i \rangle^{code} - \gamma^S \langle \varphi_i \rangle^S), \quad (\text{A4a})$$

with

$$\langle \varphi_i \rangle^S = \begin{cases} \text{const.}, & \text{if } \varphi_i \text{ is passive scalar,} \\ 0, & \text{if } \varphi_i \text{ is velocity.} \end{cases} \quad (\text{A4b})$$

Advancing this approach for the (co-)variances gives

$$\langle \varphi'_i \varphi'_j \rangle^F = \gamma^{rel} [\langle \varphi'_i \varphi'_j \rangle^0 + (1 - \gamma^{rel})(\langle \varphi_i \rangle^0 - \langle \varphi_i \rangle^S)(\langle \varphi_j \rangle^0 - \langle \varphi_j \rangle^S)], \quad (\text{A5})$$

with

$$\langle \varphi'_i \varphi'_j \rangle^0 = \frac{\langle \varphi'_i \varphi'_j \rangle^{code}}{\gamma^0} - \gamma^1 (\langle \varphi_i \rangle^1 - \langle \varphi_i \rangle^0)(\langle \varphi_j \rangle^1 - \langle \varphi_j \rangle^0), \quad (\text{A6})$$

$$\langle \varphi_i \rangle^0 = \frac{1}{\gamma^0} (\langle \varphi_i \rangle^{code} - \gamma^1 \langle \varphi_i \rangle^1), \quad (\text{A7})$$

$$\langle \varphi_i \rangle^1 = \begin{cases} \text{const.}, & \text{if } \varphi_i \text{ is passive scalar,} \\ 0, & \text{if } \varphi_i \text{ is velocity.} \end{cases} \quad (\text{A8})$$

The values of $\langle \varphi_i \rangle^S$ and $\langle \varphi_i \rangle^1$ have to be known in advance and the (co-)variances $\langle \varphi'_i \varphi'_j \rangle^S \equiv 0$ and $\langle \varphi'_i \varphi'_j \rangle^1 \equiv 0$ are always zero.

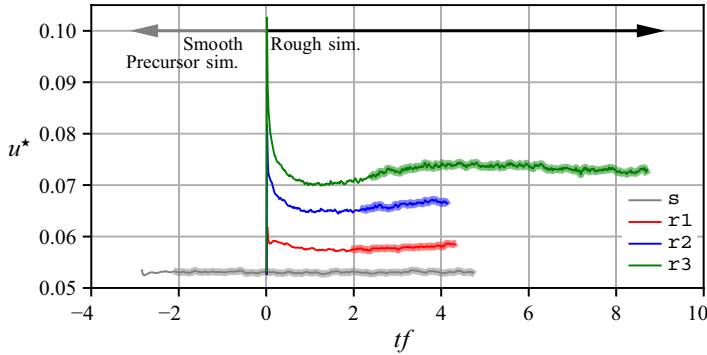


Figure 16. Temporal evolution of the friction velocity u_* for the smooth (grey) and the three rough cases (red, blue, green), with $tf = 0$ for the start of the rough cases. Thick transparent lines denote the intervals for time integration of the flow variables. Time is scaled in eddy-turnover times f^{-1} . The averaging time of cases s and $r3$ is a full inertial cycle.

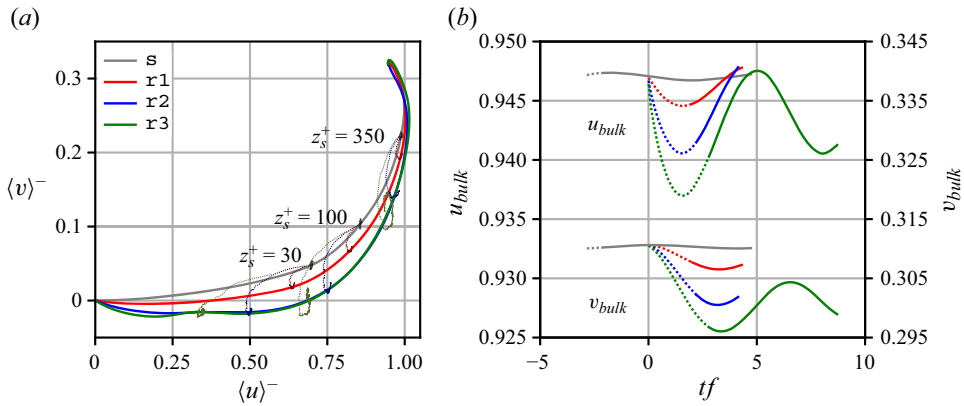


Figure 17. Inertial oscillations of the conducted cases. (a) Mean hodographs are shown with thick solid lines, and the thin lines show the temporal evolution of $\langle u \rangle$, $\langle v \rangle$ at specific heights (scaled in inner smooth units). (b) Temporal streamwise (top half) and spanwise (bottom half) bulk velocities $u_{i,bulk}(t) = L_z^{-1} \int_0^{L_z} \langle u_i(t, z) \rangle dz$, with time in eddy-turnover times f^{-1} . Dotted lines in (a) and (b) depict the initial transient of the cases, which is excluded from time averaging.

Appendix B. Time integration for statistical analysis and inertial oscillations

For initialization of the smooth case s we take the fully turbulent velocity fields of a previous simulation, which was in a statistically converged state of similar Reynolds number. Those original fields are interpolated to the current computational grid (table 1). The passive scalar of the smooth case is introduced with an initial exponentially decaying profile. The rough cases are initialized to the time instance $t = 0$ with fully turbulent, three-dimensional fields (velocities and passive scalar) from the smooth case s , and were already in a statistically converged state.

A measurement for determining statistical convergence of the cases is the temporal evolution of the friction velocity $u_*(t)$ (figure 16), following the method described in § 4.1. After an initial transient (adaptation phase of new boundary conditions), $u_*(t)$ reaches a quasi-steady state, which is determined by visual inspection, and from which flow statistics are collected for temporal integration.

Another helpful tool for diagnosing statistical convergence and gradual adaptation of the simulations to the new boundary conditions is the visualizations of inertial oscillations with the period of $2\pi/f$, which are visible in the hodographs and horizontal bulk velocities (figure 17). The smooth case s is statistically converged and therefore the amplitude of the inertial oscillation is negligible. This is also valid in the near-wall region (figure 17a). Adjusting the boundary conditions by introducing surface roughness increases inertial oscillations, which then slowly decay over time. Cases s and $r3$ are averaged over approximately one full inertial period, whereas $r1$, $r2$ are averaged over 0.4, 0.3 inertial periods.

REFERENCES

- AHN, J., LEE, J.H. & SUNG, H.J. 2013 Statistics of the turbulent boundary layers over 3D cube-roughened walls. *Intl J. Heat Fluid Flow* **44**, 394–402.
- ANDREAS, E.L. 1987 A theory for the scalar roughness and the scalar transfer coefficients over snow and sea ice. *Boundary-Layer Meteorol.* **38** (1), 159–184.
- ANDREAS, E.L., CLAFFEY, K.J., JORDAN, R.E., FAIRALL, C.W., GUEST, P.S., PERSSON, P.O.G. & GRACHEV, A.A. 2006 Evaluations of the von Kármán constant in the atmospheric surface layer. *J. Fluid Mech.* **559**, 117–149.
- ANSORGE, C. 2017 Analyses of turbulence in the neutrally and stably stratified planetary boundary layer. Springer theses, Springer International.
- ANSORGE, C. 2019 Scale dependence of atmosphere–surface coupling through similarity theory. *Boundary-Layer Meteorol.* **170** (1), 1–27.
- ANSORGE, C. & MELLADO, J.P. 2014 Global intermittency and collapsing turbulence in the stratified planetary boundary layer. *Boundary-Layer Meteorol.* **153** (1), 89–116.
- ANSORGE, C. & MELLADO, J.P. 2016 Analyses of external and global intermittency in the logarithmic layer of Ekman flow. *J. Fluid Mech.* **805** (1), 611–635.
- BARENBLATT, G.I. 1993 Scaling laws for fully developed turbulent shear flows. Part 1. Basic hypotheses and analysis. *J. Fluid Mech.* **248**, 513–520.
- BRUTSAERT, W. 1975a The roughness length for water vapor sensible heat, and other scalars. *J. Atmos. Sci.* **32** (10), 2028–2031.
- BRUTSAERT, W. 1975b A theory for local evaporation (or heat transfer) from rough and smooth surfaces at ground level. *Water Resour. Res.* **11** (4), 543–550.
- BRUTSAERT, W. 1982 *Evaporation into the Atmosphere*. Springer Netherlands.
- CASTRO, I.P. 2007 Rough-wall boundary layers: mean flow universality. *J. Fluid Mech.* **585**, 469–485.
- CASTRO, I.P. & LEONARDI, S. 2010 Very-rough-wall channel flows: a DNS study. In *IUTAM Symposium on The Physics of Wall-Bounded Turbulent Flows on Rough Walls* (ed. T. B. Nickels), IUTAM Bookseries, pp. 175–181. Springer Netherlands.
- CEBECI, T. & BRADSHAW, P. 1984 *Physical and Computational Aspects of Convective Heat Transfer. H: Hauptband*. Springer.
- CHANDRAMOULI, P., HEITZ, D., LAIZET, S. & MÉMIN, E. 2018 Coarse large-eddy simulations in a transitional wake flow with flow models under location uncertainty. *Comput. Fluids* **168**, 170–189.
- CHENG, H., HAYDEN, P., ROBINS, A.G. & CASTRO, I.P. 2007 Flow over cube arrays of different packing densities. *J. Wind Engng Ind. Aerodyn.* **95** (8), 715–740.
- CHENG, W.-C. & PORTÉ-AGEL, F. 2015 Adjustment of turbulent boundary-layer flow to idealized urban surfaces: a large-eddy simulation study. *Boundary-Layer Meteorol.* **155** (2), 249–270.
- CHORIN, A.J. 1968 Numerical solution of the Navier–Stokes equations. *Math. Comput.* **22** (104), 745–762.
- CHUNG, D., HUTCHINS, N., SCHULTZ, M.P. & FLACK, K.A. 2021 Predicting the drag of rough surfaces. *Annu. Rev. Fluid Mech.* **53** (1), 439–471.
- CLAUSER, F.H. 1954 Turbulent boundary layers in adverse pressure gradients. *J. Aeronaut. Sci.* **21** (2), 91–108.
- COCEAL, O., THOMAS, T.G., CASTRO, I.P. & BELCHER, S.E. 2006 Mean flow and turbulence statistics over groups of urban-like cubical obstacles. *Boundary-Layer Meteorol.* **121** (3), 491–519.
- COLEMAN, G.N. 1999 Similarity statistics from a direct numerical simulation of the neutrally stratified planetary boundary layer. *J. Atmos. Sci.* **56** (6), 891–900.
- COLEMAN, G.N., FERZIGER, J.H. & SPALART, P.R. 1990 A numerical study of the turbulent Ekman layer. *J. Fluid Mech.* **213**, 313–348.

- DAVIDSON, P.A. & KROGSTAD, P.-Å. 2014 A universal scaling for low-order structure functions in the log-law region of smooth- and rough-wall boundary layers. *J. Fluid Mech.* **752**, 140–156.
- DEUSEBIO, E., BRETHOUWER, G., SCHLATTER, P. & LINDBORG, E. 2014 A numerical study of the unstratified and stratified Ekman layer. *J. Fluid Mech.* **755**, 672–704.
- DIMOTAKIS, P.E. 2005 Turbulent mixing. *Annu. Rev. Fluid Mech.* **37** (1), 329–356.
- EKMAN, V.W. 1905 On the influence of the earth's rotation on ocean-currents. *Ark. Mat. Astron. Fys.* **2**, 1–53.
- FADLUN, E.A., VERZICCO, R., ORLANDI, P. & MOHD-YUSOF, J. 2000 Combined immersed-boundary finite-difference methods for three-dimensional complex flow simulations. *J. Comput. Phys.* **161** (1), 35–60.
- FANG, J., DIEBOLD, M., HIGGINS, C. & PARLANGE, M.B. 2011 Towards oscillation-free implementation of the immersed boundary method with spectral-like methods. *J. Comput. Phys.* **230** (22), 8179–8191.
- FINNIGAN, J. 2000 Turbulence in plant canopies. *Annu. Rev. Fluid Mech.* **32** (1), 519–571.
- FOKEN, T. 2006 50 years of the Monin–Obukhov similarity theory. *Boundary-Layer Meteorol.* **119** (3), 431–447.
- FORNBERG, B. 1996 *A Practical Guide to Pseudospectral Methods*. Cambridge Monographs on Applied and Computational Mathematics. Cambridge University Press.
- FRENZEN, P. & VOGEL, C.A. 1995a A further note 'on the magnitude and apparent range of variation of the von Kármán constant'. *Boundary-Layer Meteorol.* **75** (3), 315–317.
- FRENZEN, P. & VOGEL, C.A. 1995b On the magnitude and apparent range of variation of the von Kármán constant in the atmospheric surface layer. *Boundary-Layer Meteorol.* **72** (4), 371–392.
- GARRATT, J.R. 1992 *The Atmospheric Boundary Layer*. Cambridge Atmospheric and Space Science Series. Cambridge University Press.
- GAUTIER, R., BIAU, D. & LAMBALLAIS, E. 2013 A reference solution of the flow over a circular cylinder at $Re = 40$. *Comput. Fluids* **75**, 103–111.
- GAUTIER, R., LAIZET, S. & LAMBALLAIS, E. 2014 A DNS study of jet control with microjets using an immersed boundary method. *Int'l J. Comput. Fluid Dyn.* **28** (6–10), 393–410.
- GIANNENAS, A.E. & LAIZET, S. 2021 A simple and scalable immersed boundary method for high-fidelity simulations of fixed and moving objects on a Cartesian mesh. *Appl. Math. Model.* **99**, 606–627.
- GOLDSTEIN, D., HANDLER, R. & SIROVICH, L. 1993 Modeling a no-slip flow boundary with an external force field. *J. Comput. Phys.* **105** (2), 354–366.
- GRIMMOND, C.S.B. & OKE, T.R. 1999 Aerodynamic properties of urban areas derived from analysis of surface form. *J. Appl. Meteorol. Climatol.* **38** (9), 1262–1292.
- HAMA, F.R. 1954 Boundary layer characteristics for smooth and rough surfaces. *Trans. Soc. Nav. Archit. Mar. Engrs* **62**, 333–358.
- HUSSAIN, M. & LEE, B.E. 1980 A wind tunnel study of the mean pressure forces acting on large groups of low-rise buildings. *J. Wind Engng Ind. Aerodyn.* **6** (3–4), 207–225.
- JAYARAMAN, B. & KHAN, S. 2020 Direct numerical simulation of turbulence over two-dimensional waves. *AIP Adv.* **10** (2), 025034.
- JIANG, Q., WANG, S. & SULLIVAN, P. 2018 Large-eddy simulation study of log laws in a neutral Ekman boundary layer. *J. Atmos. Sci.* **75** (6), 1873–1889.
- JIMÉNEZ, J. 2004 Turbulent flows over rough walls. *Annu. Rev. Fluid Mech.* **36** (1), 173–196.
- JOHANSSON, A.V. & WIKSTRÖM, P.M. 2000 DNS and modelling of passive scalar transport in turbulent channel flow with a focus on scalar dissipation rate modelling. *Flow Turbul. Combust.* **63** (1), 223–245.
- KADER, B.A. 1981 Temperature and concentration profiles in fully turbulent boundary layers. *Int'l J. Heat Mass Transfer* **24** (9), 1541–1544.
- KADIVAR, M., TORMEY, D. & MCGRANAGHAN, G. 2021 A review on turbulent flow over rough surfaces: fundamentals and theories. *Int'l J. Thermofluids* **10**, 100077.
- KANDA, M., INAGAKI, A., MIYAMOTO, T., GRYSCHKA, M. & RAASCH, S. 2013 A new aerodynamic parametrization for real urban surfaces. *Boundary-Layer Meteorol.* **148** (2), 357–377.
- KANDA, M., KANEGA, M., KAWAI, T., MORIWAKI, R. & SUGAWARA, H. 2007 Roughness lengths for momentum and heat derived from outdoor urban scale models. *J. Appl. Meteorol. Climatol.* **46** (7), 1067–1079.
- KANDA, M., MORIWAKI, R. & KASAMATSU, F. 2004 Large-eddy simulation of turbulent organized structures within and above explicitly resolved cube arrays. *Boundary-Layer Meteorol.* **112** (2), 343–368.
- KASAGI, N., TOMITA, Y. & KURODA, A. 1992 Direct numerical simulation of passive scalar field in a turbulent channel flow. *J. Heat Transfer* **114** (3), 598–606.
- KAWAMURA, H., ABE, H. & MATSUO, Y. 1999 DNS of turbulent heat transfer in channel flow with respect to Reynolds and Prandtl number effects. *Int'l J. Heat Fluid Flow* **20** (3), 196–207.

- KAWAMURA, H., ABE, H. & SHINGAI, K. 2000 DNS of turbulence and heat transport in a channel flow with different Reynolds and Prandtl numbers and boundary conditions. *Proceedings of the 3rd International Symposium on Turbulence, Heat and Mass Transfer* (ed. Y. Nagano), pp. 15–32. Engineering Foundation.
- KHAN, S. & JAYARAMAN, B. 2019 Statistical structure and deviations from equilibrium in wavy channel turbulence. *Fluids* **4** (3), 161.
- KIM, J., KIM, D. & CHOI, H. 2001 An immersed-boundary finite-volume method for simulations of flow in complex geometries. *J. Comput. Phys.* **171** (1), 132–150.
- KOLMOGOROV, A.N. 1941 Dissipation of energy in locally isotropic turbulence. *Dokl Akad. Nauk SSSR* **434** (1890), 15–17.
- KOSTELECKY, J. & ANSORGE, C. 2024 Direct numerical simulation of turbulent Ekman flow with cubic small-scale surface roughness ($Re = 1000$). <http://dx.doi.org/10.17169/refubium-43215>.
- LAIZET, S. & LAMBALLAIS, E. 2009 High-order compact schemes for incompressible flows: a simple and efficient method with quasi-spectral accuracy. *J. Comput. Phys.* **228** (16), 5989–6015.
- LAMBALLAIS, É. & SILVESTRINI, J. 2002 Direct numerical simulation of interactions between a mixing layer and a wake around a cylinder. *J. Turbul.* **3**, 28.
- LEE, J., KIM, J., CHOI, H. & YANG, K.-S. 2011a Sources of spurious force oscillations from an immersed boundary method for moving-body problems. *J. Comput. Phys.* **230** (7), 2677–2695.
- LEE, J.H., SUNG, H.J. & KROGSTAD, P.-Å. 2011b Direct numerical simulation of the turbulent boundary layer over a cube-roughened wall. *J. Fluid Mech.* **669**, 397–431.
- LEE, S., GOHARI, S.M.I. & SARKAR, S. 2020 Direct numerical simulation of stratified Ekman layers over a periodic rough surface. *J. Fluid Mech.* **902**, A25.
- LELE, S.K. 1992 Compact finite difference schemes with spectral-like resolution. *J. Comput. Phys.* **103** (1), 16–42.
- LEONARDI, S. & CASTRO, I.P. 2010 Channel flow over large cube roughness: a direct numerical simulation study. *J. Fluid Mech.* **651**, 519–539.
- LI, D., RIGDEN, A., SALVUCCI, G. & LIU, H. 2017 Reconciling the Reynolds number dependence of scalar roughness length and laminar resistance. *Geophys. Res. Lett.* **44** (7), 3193–3200.
- LI, Q. & BOU-ZEID, E. 2019 Contrasts between momentum and scalar transport over very rough surfaces. *J. Fluid Mech.* **880**, 32–58.
- LI, Q., BOU-ZEID, E. & ANDERSON, W. 2016 The impact and treatment of the Gibbs phenomenon in immersed boundary method simulations of momentum and scalar transport. *J. Comput. Phys.* **310**, 237–251.
- LI, Q., BOU-ZEID, E., GRIMMOND, S., ZILITINKEVICH, S. & KATUL, G. 2020 Revisiting the relation between momentum and scalar roughness lengths of urban surfaces. *Q. J. R. Meteorol. Soc.* **146** (732), 3144–3164.
- MARUSIC, I., MONTY, J.P., HULTMARK, M. & SMITS, A.J. 2013 On the logarithmic region in wall turbulence. *J. Fluid Mech.* **716**, R3.
- MELLADO, J.P. & ANSORGE, C. 2012 Factorization of the Fourier transform of the pressure-Poisson equation using finite differences in collocated grids. *Z. Angew. Math. Mech.* **92** (5), 380–392.
- MIYASHITA, K., IWAMOTO, K. & KAWAMURA, H. 2006 Direct numerical simulation of the neutrally stratified turbulent Ekman boundary layer. *J. Earth Simul.* **6**, 3–15.
- MOHD-YUSOF, J. 1997 Combined immersed boundaries/B-splines methods for simulations of flows in complex geometries. *Center for Turbulence Research*, pp. 317–327.
- MONIN, A.S. 1970 The atmospheric boundary layer. *Annu. Rev. Fluid Mech.* **2**, 225–250.
- NAGIB, H.M. & CHAUHAN, K.A. 2008 Variations of von Kármán coefficient in canonical flows. *Phys. Fluids* **20** (10), 101518.
- NIKURADSE, J. 1933 Laws of flow in rough pipes. *NACA Tech. Memorandum* 1295, 1–62.
- OBUKHOV, A.M. 1941 O Raspredelenie energii w spektre turbulentnowo potoka. *Isv. Akad. Nauk SSSR* **1941** (4–5), 453–466.
- PARNAUDEAU, P., CARLIER, J., HEITZ, D. & LAMBALLAIS, E. 2008 Experimental and numerical studies of the flow over a circular cylinder at Reynolds number 3900. *Phys. Fluids* **20** (8), 085101.
- PARNAUDEAU, P., LAMBALLAIS, E., HEITZ, D. & SILVESTRINI, J.H. 2004 Combination of the immersed boundary method with compact schemes for DNS of flows in complex geometry. In *Direct and Large-Eddy Simulation V* (ed. R. Friedrich, B.J. Geurts & O. Métais), ERCOFTAC Series, pp. 581–590. Springer Netherlands.
- PERRET, L., BASLEY, J., MATHIS, R. & PIQUET, T. 2019 The atmospheric boundary layer over urban-like terrain: influence of the plan density on roughness sublayer dynamics. *Boundary-Layer Meteorol.* **170** (2), 205–234.

- PIROZZOLI, S., BERNARDINI, M. & ORLANDI, P. 2016 Passive scalars in turbulent channel flow at high Reynolds number. *J. Fluid Mech.* **788**, 614–639.
- PIROZZOLI, S., ROMERO, J., FATICA, M., VERZICCO, R. & ORLANDI, P. 2022 DNS of passive scalars in turbulent pipe flow. *J. Fluid Mech.* **940**, A45.
- PLACIDI, M. & GANAPATHISUBRAMANI, B. 2015 Effects of frontal and plan solidities on aerodynamic parameters and the roughness sublayer in turbulent boundary layers. *J. Fluid Mech.* **782**, 541–566.
- POPE, S.B. 2000 *Turbulent Flows*. Cambridge University Press.
- PRANDTL, L. 1961 Zur turbulenten Strömung in Röhren und längs Platten. In *Ludwig Prandtl Gesammelte Abhandlungen* (ed. W. Tollmien, H. Schlichting, H. Görtler & F.W. Riegels). Springer Berlin Heidelberg.
- RAUPACH, M.R., ANTONIA, R.A. & RAJAGOPALAN, S. 1991 Rough-wall turbulent boundary layers. *Appl. Mech. Rev.* **44** (1), 1–25.
- RESSEGUIER, V., MÉMIN, E., HEITZ, D. & CHAPRON, B. 2017 Stochastic modelling and diffusion modes for proper orthogonal decomposition models and small-scale flow analysis. *J. Fluid Mech.* **826**, 888–917.
- ROSSBY, C.-G. & MONTGOMERY, R.B. 1935 The layer of frictional influence in wind and ocean currents. *Pap. Phys. Oceanogr. Meteorol.* **III** (3), 1–101.
- RUNGE, C. 1901 Über empirische Funktionen und die Interpolation zwischen äquidistanten Ordinaten. *Z. Math. Phys.* **46**, 224–243.
- SCHÄFER, K., FOROOGHI, P., STRAUB, S., FROHNAPFEL, B. & STROH, A. 2020 Direct numerical simulations of a turbulent flow over wall-mounted obstacles – a comparison of different numerical approaches. In *Direct and Large Eddy Simulation XII* (ed. M. García-Villalba, H. Kuerten & M.V. Salvetti), vol. 27, pp. 91–96. Springer International.
- SCHÄFER, K., FROHNAPFEL, B. & MELLADO, J.P. 2022a The effect of spanwise heterogeneous surfaces on mixed convection in turbulent channels. *J. Fluid Mech.* **950**, A22.
- SCHÄFER, K., STROH, A., FOROOGHI, P. & FROHNAPFEL, B. 2022b Modelling spanwise heterogeneous roughness through a parametric forcing approach. *J. Fluid Mech.* **930**, A7.
- SCHÄFER, K., STROH, A., FROHNAPFEL, B. & GATTI, D. 2019 Investigation of turbulent budgets in channels with secondary motions induced by streamwise-aligned ridges. In *11th International Symposium on Turbulence and Shear Flow Phenomena (TSFP11)*, Southampton, UK, July 30–August 2, 2019.
- SCHLICHTING, H. 1936 Experimentelle Untersuchungen zum Rauigkeitsproblem. *Ingenieur-Archiv* **7** (1), 1–34.
- SHAH, S.K. & BOU-ZEID, E. 2014 Direct numerical simulations of turbulent Ekman layers with increasing static stability: modifications to the bulk structure and second-order statistics. *J. Fluid Mech.* **760**, 494–539.
- SHAO, Y. & YANG, Y. 2008 A theory for drag partition over rough surfaces. *J. Geophys. Res.* **113** (F2), F02S05.
- SHINGAI, K. & KAWAMURA, H. 2004 A study of turbulence structure and large-scale motion in the Ekman layer through direct numerical simulations. *J. Turbul.* **5** (1), 013.
- SPALART, P.R. 1989 Theoretical and numerical study of a three-dimensional turbulent boundary layer. *J. Fluid Mech.* **205**, 319.
- SPALART, P.R., COLEMAN, G.N. & JOHNSTONE, R. 2008 Direct numerical simulation of the Ekman layer: a step in Reynolds number, and cautious support for a log law with a shifted origin. *Phys. Fluids* **20** (10), 101507.
- SPALART, P.R., COLEMAN, G.N. & JOHNSTONE, R. 2009 Retraction: ‘Direct numerical simulation of the Ekman layer: a step in Reynolds number, and cautious support for a log law with a shifted origin’ [*Phys. Fluids* 20, 101507 (2008)]. *Phys. Fluids* **21** (10), 109901.
- SQUIRE, D.T., MORRILL-WINTER, C., HUTCHINS, N., SCHULTZ, M.P., KLEWICKI, J.C. & MARUSIC, I. 2016 Comparison of turbulent boundary layers over smooth and rough surfaces up to high Reynolds numbers. *J. Fluid Mech.* **795**, 210–240.
- STOESSER, T., MATHEY, F., FRÖHLICH, J. & RODI, W. 2003 LES of flow over multiple cubes. ERCOFTAC Bulletin no. 56, 15–19.
- STULL, R.B. 1988 *An Introduction to Boundary Layer Meteorology*. Atmospheric Sciences Library. Kluwer Academic Publishers.
- SUBRAMANIAN, C.S. & ANTONIA, R.A. 1981 Effect of Reynolds number on a slightly heated turbulent boundary layer. *Intl J. Heat Mass Transfer* **24** (11), 1833–1846.
- TÉMAM, R. 1969 Sur l’approximation de la solution des équations de Navier–Stokes par la méthode des pas fractionnaires (II). *Arch. Ration Mech. Anal.* **33** (5), 377–385.
- TENNEKES, H. & LUMLEY, J.L. 1972 *A First Course in Turbulence*. MIT Press.
- THEOBALD, F., SCHÄFER, K., YANG, J., FROHNAPFEL, B., STRIPF, M., FOROOGHI, P. & STROH, A. 2021 Comparison of different solvers and geometry representation strategies for DNS of rough wall channel flow. In *14th WCCM-ECCOMAS Congress*. CIMNE.

Small-scale roughness in Ekman flow

- TOWNSEND, A.A. 1961 Equilibrium layers and wall turbulence. *J. Fluid Mech.* **11** (1), 97–120.
- TOWNSEND, A.A. 1976 *The Structure of Turbulent Shear Flow*, 2nd edn. Cambridge University Press.
- TSENG, Y.-H., MENEVEAU, C. & PARLANGE, M.B. 2006 Modeling flow around bluff bodies and predicting urban dispersion using large eddy simulation. *Environ. Sci. Technol.* **40** (8), 2653–2662.
- VON KÁRMÁN, T. 1930 Mechanische Ähnlichkeit und turbulenz. *Nachr. Ges. Wiss. Göttingen* **1930**, 58–76.
- WILLIAMSON, J.H. 1980 Low-storage Runge–Kutta schemes. *J. Comput. Phys.* **35** (1), 48–56.
- XIAO, H., WU, J.-L., LAIZET, S. & DUAN, L. 2020 Flows over periodic hills of parameterized geometries: a dataset for data-driven turbulence modeling from direct simulations. *Comput. Fluids* **200**, 104431.
- XIE, Z.-T., COCEAL, O. & CASTRO, I.P. 2008 Large-eddy simulation of flows over random urban-like obstacles. *Boundary-Layer Meteorol.* **129** (1), 1–23.
- YANG, X.I.A., SADIQUE, J., MITTAL, R. & MENEVEAU, C. 2016 Exponential roughness layer and analytical model for turbulent boundary layer flow over rectangular-prism roughness elements. *J. Fluid Mech.* **789**, 127–165.
- ZANOUN, E.-S., DURST, F. & NAGIB, H. 2003 Evaluating the law of the wall in two-dimensional fully developed turbulent channel flows. *Phys. Fluids* **15** (10), 3079–3089.
- ZILITINKEVICH, S. 1995 Non-local turbulent transport: pollution dispersion aspects of coherent structure of connective flows. In *Air Pollution 1995*, pp. 53–60. Porto Carras.